The Astrophysical Journal Supplement Series, 229:32 (31pp), 2017 April https://doi.org/10.3847/1538-4365/aa66cb

CANDELS Multi-wavelength Catalogs: Source Identification and Photometry in the CANDELS Extended Groth Strip

Mauro Stefanon[1,2], Haojing Yan[2], Bahram Mobasher[3], Guillermo Barro[4,5], Jennifer L. Donley[6], Adriano Fontana[7], Shoubaneh Hemmati[8], Anton M. Koekemoer[9], BoMee Lee[10], Seong-Kook Lee[11], Hooshang Nayyeri[3,12], Michael Peth[13], Janine Pforr[14], Mara Salvato[15], Tommy Wiklind[16], Stijn Wuyts[17], Matthew L. N. Ashby[18], Marco Castellano[7], Christopher J. Conselice[19], Michael C. Cooper[12], Asantha R. Cooray[12], Timothy Dolch[20], Henry Ferguson[9], Audrey Galametz[7,15], Mauro Giavalisco[10], Yicheng Guo[4], Steven P. Willner[18], Mark E. Dickinson[21], Sandra M. Faber[4], Giovanni G. Fazio[18], Jonathan P. Gardner[22], Eric Gawiser[23], Andrea Grazian[7], Norman A. Grogin[9], Dale Kocevski[24], David C. Koo[4], Kyoung-Soo Lee[25], Ray A. Lucas[9], Elizabeth J. McGrath[24], Kirpal Nandra[15,26], Jeffrey A. Newman[27], and Arjen van der Wel[28]

[1] Leiden Observatory, Leiden University, NL-2300 RA Leiden, The Netherlands; stefanon@strw.leidenuniv.nl
[2] Department of Physics and Astronomy, University of Missouri, Columbia, MO 65211, USA
[3] Department of Physics and Astronomy, University of California, Riverside, CA 92521, USA
[4] UCO/Lick Observatory, Department of Astronomy and Astrophysics, University of California, Santa Cruz, CA 95064, USA
[5] Department of Astronomy, University of California at Berkeley, Berkeley, CA 94720-3411, USA
[6] Los Alamos National Laboratory, Los Alamos, NM 87544, USA
[7] INAF—Osservatorio Astronomico di Roma, via Frascati 33, I-00040 Monte Porzio Catone (RM), Italy
[8] Infrared Processing and Analysis Center, California Institute of Technology, MS 100-22, Pasadena, CA 91125, USA
[9] Space Telescope Science Institute, 3700 San Martin Drive, Baltimore, MD 21218, USA
[10] Department of Astronomy, University of Massachusetts, 710 North Plesant Street, Amherst, MA 01003, USA
[11] Center for the Exploration of the Origin of the Universe (CEOU), Department of Physics and Astronomy, Seoul National University, Seoul, Korea
[12] Department of Physics and Astronomy, University of California, Irvine, CA 92697, USA
[13] Department of Physics and Astronomy, The Johns Hopkins University, 366 Bloomberg Center, Baltimore, MD 21218, USA
[14] Aix Marseille Université, CNRS, LAM (Laboratoire d'Astrophysique de Marseille) UMR 7326, F-13388, Marseille, France
[15] Max-Planck-Institut fur Extraterrestrische Physik, Giessenbachstrasse 1, D-85748 Garching bei Munchen, Germany
[16] Department of Physics, Catholic University of America, Washington, DC 20064, USA
[17] Department of Physics, University of Bath, Claverton Down, Bath, BA2 7AY, UK
[18] Harvard Smithsonian Center for Astrophysics, 60 Garden Street, MS-66, Cambridge, MA 02138-1516, USA
[19] School of Physics and Astronomy, University of Nottingham, Nottingham, UK
[20] Deptartment of Physics, Hillsdale College, 33 E. College Street, Hillsdale, MI 49242, USA
[21] National Optical Astronomy Observatories, 950 N Cherry Avenue, Tucson, AZ 85719, USA
[22] NASA's Goddard Space Flight Center, Greenbelt, MD 20771, USA
[23] Department of Physics and Astronomy, Rutgers, The State University of New Jersey, 136 Frelinghuysen Road, Piscataway, NJ 08854, USA
[24] Department of Physics and Astronomy, Colby College, Waterville, ME 04901, USA
[25] Department of Physics, Purdue University, 525 Northwestern Avenue, West Lafayette, USA
[26] Astrophysics Group, Blackett Laboratory, Imperial College London, London SW7 2AZ, UK
[27] Department of Physics and Astronomy and PITT PACC, University of Pittsburgh, Pittsburgh, PA 15260, USA
[28] Max-Planck Institute for Astronomy, D-69117 Heidelberg, Germany
Received 2015 November 16; revised 2016 September 12; accepted 2016 September 12; published 2017 April 3

Abstract

We present a 0.4–8 μm multi-wavelength photometric catalog in the Extended Groth Strip (EGS) field. This catalog is built on the *Hubble Space Telescope (HST)* WFC3 and ACS data from the Cosmic Assembly Near-infrared Deep Extragalactic Legacy Survey (CANDELS), and it incorporates the existing *HST* data from the All-wavelength Extended Groth strip International Survey (AEGIS) and the 3D-*HST* program. The catalog is based on detections in the F160W band reaching a depth of F160W = 26.62 AB (90% completeness, point sources). It includes the photometry for 41,457 objects over an area of $\approx$206 arcmin^2 in the following bands: *HST*/ACS F606W and F814W; *HST* WFC3 F125W, F140W, and F160W; Canada–France–Hawaii Telescope (CFHT)/Megacam u^*, g', r', i' and z'; CFHT/WIRCAM J, H, and K_S; Mayall/NEWFIRM $J1$, $J2$, $J3$, $H1$, $H2$, and K; *Spitzer* IRAC 3.6, 4.5, 5.8, and 8.0 μm. We are also releasing value-added catalogs that provide robust photometric redshifts and stellar mass measurements. The catalogs are publicly available through the CANDELS repository.

Key words: catalogs – galaxies: evolution – galaxies: photometry – methods: data analysis – techniques: photometric

Supporting material: machine-readable tables

1. Introduction

The Cosmic Assembly Near-infrared Deep Extragalactic Legacy Survey (CANDELS; Grogin et al. 2011; Koekemoer et al. 2011) is a 902-orbit *Hubble Space Telescope* (*HST*) Multi-Cycle Treasury (MCT) program aimed at obtaining deep multi-wavelength photometric data for more than a quarter million objects. Observations followed a two-tiered strategy and were distributed over five fields.

The deeper layer of our survey (CANDELS Deep) covers $\sim$130 arcmin^2 to a depth of 27.6–29.4 AB (5σ limit for point sources) over the north and south fields of the Great Observatories Origins Deep Survey (Giavalisco et al. 2004). Its photometric depth has already been shown to be capable of reaching $0.5L^*$ galaxies at $z \gtrsim 8$ (see, e.g., Bouwens et al. 2015; Finkelstein et al. 2015) and also to cover the low-mass end of the galaxy population at $z \sim$ 2–5 (e.g., Duncan et al.

2014; Tomczak et al. 2014; Grazian et al. 2015; Mortlock et al. 2015). The shallower layer of the survey (CANDELS Wide) extends the coverage to a total of ∼720 arcmin^2 down to a depth of 26.9–28.9 AB in five fields, namely GOODS-N, GOODS-S, the Extended Groth Strip (EGS; Davis et al. 2007), the Cosmic Evolution Survey field (COSMOS; Scoville et al. 2007), and the Ultra Deep Survey field (UDS; Cirasuolo et al. 2007; Lawrence et al. 2007). Furthermore, the combination of photometric depth and covered area allow for the detection of potential luminous high-z galaxies, primary targets for follow-up observations with, e.g., *HST*, the Atacama Large Millimeter/submillimeter Array (ALMA) and the *James Webb Space Telescope* (see, e.g., Yan et al. 2012; Oesch et al. 2015).

The multi-wavelength photometric catalogs for the GOODS-S and UDS fields have already been presented by Guo et al. (2013) and Galametz et al. (2013), respectively; photometric redshifts and stellar population parameters for these two fields are described by Dahlen et al. (2013) and Santini et al. (2015), respectively. The CANDELS GOODS-S data, combined with the medium bands from Subaru (Cardamone et al. 2010), were also used in Hsu et al. (2014) to compute photometric redshifts of normal galaxies and AGNs. The description of the multi-wavelength catalogs, photometric redshifts, and stellar population parameters for the COSMOS and GOODS-N fields are presented by Nayyeri et al. (2017) and G. Barro et al. (2017, in preparation), respectively. This paper presents the CANDELS multi-wavelength photometric catalog for the EGS field. Companion papers will present the rest-frame luminosities (D. Kocevski et al. 2016, in preparation) and the probability distribution functions of photometric redshifts (D. Kodra et al. 2016, in preparation). Since the first observations (Rhodes et al. 2000, PI Groth 1994), the EGS has been the site of several surveys, notably the All-wavelength Extended Groth Strip International Survey (AEGIS, Davis et al. 2007) and the DEEP2+3 spectroscopic survey (Coil et al. 2004; Cooper et al. 2006, 2011, 2012; Newman et al. 2013). The catalog is complemented by measurements of the photometric redshifts and stellar population parameters.

This paper is organized as follows. Section 2 describes the data sets used to construct our multi-wavelength catalog. Section 3 discusses the World Coordinate System (WCS) for the *HST* mosaics. Section 4 describes the procedures for the flux measurements over the wide wavelength range, while Section 5 presents the validation tests of the multi-wavelength catalog. Section 6 presents the photometric redshift and stellar mass measurements. Our results are summarized in Section 7. Our catalogs are accessible on the primary CANDELS pages at MAST,[29] through the Vizier service,[30] and from the CANDELS team project website.[31]

All magnitudes are given in the AB system. We adopted a standard cosmology with $H_0 = 70$ km s^{-1} Mpc^{-1}, $\Omega_\Lambda = 0.7$, and $\Omega_m = 0.3$.

2. Data

The CANDELS EGS field is centered at $\alpha(J2000) = 14^h17^m00^s$ and $\delta(J2000) = +52°30'00''$, corresponding to high Galactic latitudes ($b \sim 60°$). The AEGIS project provided deep *HST*/ACS imaging data in the F606W and F814W bands to 5σ depths of 28.7 and 28.1 mag, respectively. The CANDELS survey adds deep *HST* WFC3 F125W and F160W coverage, and increases the depth of the ACS F606W and F814W mosaics with new data from parallel observations (Grogin et al. 2011; Koekemoer et al. 2011).

The wavelength coverage is complemented by extensive ground- and space-based imaging: UV data from *GALEX* (PI C. Martin); u^*, g', r', i, z' from Canada–France–Hawaii Telescope (CFHT)/MegaCam observations; *B*-, *R*-, and *I*-band imaging obtained with the CFHT 12 K mosaic camera (Cuillandre et al. 2001; Coil et al. 2004); near-infrared (NIR) broadband *J*, *H*, and K_S imaging from the WIRCam Deep Survey (WIRDS; Bielby et al. 2012); *J*- and *K*-band data from the Palomar Observatory Wide-Field Infrared Survey (Conselice et al. 2008); medium-band NIR filters from the NEWFIRM camera (van Dokkum et al. 2009); *HST* WFC3 F140W data from the 3D-*HST* survey (PI van Dokkum; Skelton et al. 2014); IRAC maps from *Spitzer* SEDS (Ashby et al. 2013) and S-CANDELS (Ashby et al. 2015); MIPS data from FIDEL (PI: M. Dickinson); *Herschel* PACS 100 and 160 μm (Lutz et al. 2011) and HerMES SPIRE 250, 350, 500 μm (Oliver et al. 2010) and 1.4 and 4.8 GHz VLA data (Willner et al. 2006; Ivison et al. 2007).

The field also benefits from substantial integration time (∼800 ks) in X-ray by *Chandra* (Laird et al. 2009; Nandra et al. 2015).[32] The area covered by the CANDELS EGS footprint also has spectroscopic coverage from the DEEP2 survey (Coil et al. 2004; Cooper et al. 2006; Newman et al. 2013). Although spectroscopically incomplete, this survey provides redshift information for $\sim 5 \times 10^4$ objects brighter than $R < 24.1$ AB (corresponding to approximately $z < 1.4$), ∼1400 of which fall within the CANDELS EGS boundaries. The recently concluded DEEP3 survey (Cooper et al. 2011, 2012) increases the number of spectrscopic redshifts in the CANDELS EGS field to a total of ∼2200. Furthermore, the 3D-*HST* project provides *HST* G141 slitless grism spectroscopy over the F140W footprint.

The multi-wavelength photometric catalog presented in this work is assembled using data spanning from 0.4 to 8 μm, taken by six different instruments. Specifically, the CANDELS EGS photometric catalog is built using the data from CFHT/MegaCam, NEWFIRM/NEWFIRM Medium-Band Survey (NMBS), CFHT/WIRCAM, *HST*/ACS, *HST*/WFC3, and *Spitzer*/IRAC. Figure 1 presents the response curves of the involved passbands, which are the convolution products of the filter transmissions and the detector throughputs. In thd case of the ground-based instruments, the atmospheric transmissions are also convolved. Table 1 summarizes the main properties of each data set. Similar to all the rest of the CANDELS fields (Guo et al. 2013; Galametz et al. 2013; G. Barro et al. 2017, in preparation; Nayyeri et al. 2017), object detection was performed on the WFC3/F160W-band image. This mosaic is fully covered by all the adopted data sets, with the exception of the data from the NMBS and the WFC3 F140W mosaic, which cover only about one-third and two-thirds of the F160W field respectively (see Figure 2).

2.1. HST

The *HST* data set consists of both optical and NIR images, which were taken by the ACS/WFC and the WFC3/IR

[29] https://archive.stsci.edu/prepds/candels
[30] http://vizier.u-strasbg.fr/viz-bin/VizieR
[31] http://candels.ucolick.org

[32] See also http://www.mpe.mpg.de/XraySurveys/AEGIS-X/.

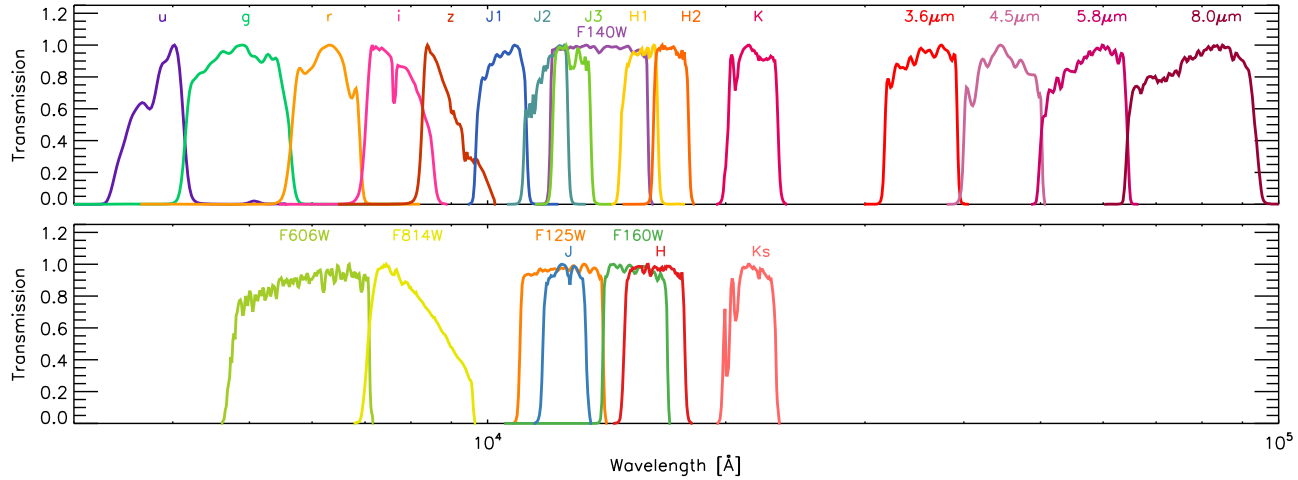

Figure 1. Response curves of the 22 bands included in the CANDELS EGS multi-wavelength catalog normalized to a maximum value of unity. The response curves are organized over two vertically stacked panels for ease of presentation. The responses correspond to the filter transmission combined with the detector quantum efficiency as well as atmospheric transmission in the case of ground-based instruments.

instruments, respectively. The WFC3 images were mostly obtained by the CANDELS program in Cycles 18 and 20. The ACS images consist of those obtained in the coordinated parallel mode during the CANDELS WFC3 observations and those from the AEGIS program obtained in Cycle 13 (Davis et al. 2007). A detailed description of *HST* data acquisition and reduction is presented by Grogin et al. (2011) and Koekemoer et al. (2011). We briefly summarize the main features below.

The AEGIS ACS data were taken in a mosaic pattern of contiguous tiles, covering an effective area of $10\farcm1 \times 70\farcm5$ in the F606W and the F814W bands. The major axis of the rectangular area has a position angle of 40°. The nominal exposure time was one orbit (∼2000 s) per filter.

The CANDELS WFC3 observations were performed within the AEGIS ACS footprint, using a rectangular grid of 3×15 tiles and forming a contiguous field of $6\farcm7 \times 30\farcm6$ at a position angle of 42°. Each tile was observed in two epochs, separated by roughly 52 days and at different orientations (by 22°). During each epoch, a given tile nominally received one orbit of observing time (∼2000 s).[33] Each orbit was shared between the F160W and the F125W filters such that $\sim 2/3$ of the orbit was assigned to the former and $\sim 1/3$ to the latter, respectively. The observation in each filter within a given orbit was always divided into two sub-exposures. With the existing AEGIS ACS data in mind, the contemporaneous CANDELS ACS parallel observations were taken in the F814W band during the first epoch and split evenly between the F606W and the F814W bands during the second epoch. As the ACS/WFC has a factor of 1.55× larger field of view than the WFC3/IR, the CANDELS ACS tiles overlapped heavily due to the abutting WFC3/IR tiling, and hence effectively resulted in two-orbit and one-orbit exposures per pixel in F814W and F606W, respectively.

The WFC3 and ACS data were all reduced and combined following the approaches described by Koekemoer et al. (2011). The image mosaics used in this work have a scale of 60 mas pixel^{-1} and all have the same WCS. The WFC3 IR mosaics have nominal exposure times of ∼1300 and ∼2700 s in F125W and F160W, respectively. The ACS mosaics incorporate the contemporaneous CANDELS data and the earlier AEGIS data and have nominal exposure times of ∼6000 and 12,000 s in F606W and F814W, respectively, reaching AB = 28.8 and 28.2 mag (5σ in apertures of $0\farcs24$ diameter, corresponding to 2× the full width at half maximum (FWHM) of the point-spread function (PSF)).

We also incorporated the WFC3 F140W images from the 3D-*HST* program (van Dokkum et al. 2011; Brammer et al. 2012; Skelton et al. 2014). The 3D-*HST* survey was an *HST* Treasury program that offered spectroscopic and photometric data in the CANDELS fields over a combined area of ∼625 arcmin^2. 3D-*HST* obtained imaging in the WFC3 F140W filter as well as spatially resolved spectroscopy with the WFC3 G141 grism. In the EGS field, the F140W imaging covered $\sim 2/3$ of the CANDELS F160W footprint (see Figure 2) and reached an average 5σ depth of 25.8 mag (in a $1''$-diameter aperture). We used the v4.1 F140W mosaic produced by the 3D-*HST* team,[34] which has the same WCS as the CANDELS WFC3 mosaics (see also Table 5 in Koekemoer et al. 2011).

2.2. Ground-based Data

2.2.1. CFHTLS

The catalog incorporates flux measurements from the broadband u^*, g', r', i', and z' images obtained by the Megacam instrument at the 3.6 m CFHT. These data correspond to the D3 field of the Deep component of the CFHT Legacy Survey (CFHTLS); the field is 1 deg^2 in size and completely covers the CANDELS EGS field.

For this work, we adopted the mosaics generated by the MegaPipe pipeline (Gwyn 2008) as described by Gwyn (2012). The sensitivity limits corresponding to the 50% completeness are $u^* = 27.5$, $g' = 27.9$, $r' = 27.6$, $i' = 27.3$, and $z' = 26.4$ mag, for the five bands respectively (Gwyn 2012). They were obtained by adding artificial point sources to the image after replacing the pixels of all the detected objects with a realization of noise and recovering sources using SExtractor (Bertin & Arnouts 1996). The image quality is homogeneous across the bands, with the PSF FWHM average values of $\sim 0\farcs7$–$0\farcs9$.

[33] The integration time in the WFC3 IR bands for nine of the tiles was reduced by 410 s in each orbit due to the WFC3 UVIS observations for the supernovae search; see Grogin et al. (2011) for details.

[34] http://3dhst.research.yale.edu/Data.php

Table 1
Summary of Photometric Data

Filter Name	Filter λ_{eff} (Å)	Filter FWHM (Å)	PSF FWHM (arcsec)	Depth[a] 5σ (AB)	ZP[b] (AB)	Astrometric System	References
CFHT/MegaCam u^*	383	61	0.95	27.1	30.0	NOMAD+SDSS	Gwyn (2012)
CFHT/MegaCam g'	489	144	0.90	27.3	30.0	⋯	⋯
CFHT/MegaCam r'	625	122	0.77	27.2	30.0	⋯	⋯
CFHT/MegaCam i'	769	138	0.71	27.0	30.0	⋯	⋯
CFHT/MegaCam z'	888	87	0.71	26.1	30.0	⋯	⋯
Mayall/NEWFIRM $J1$	1047	150	1.13	24.4	23.31	NOMAD+SDSS[c]	Whitaker et al. (2011)
Mayall/NEWFIRM $J2$	1195	151	1.16	24.1	23.35	⋯	⋯
Mayall/NEWFIRM $J3$	1279	140	1.08	24.0	23.37	⋯	⋯
Mayall/NEWFIRM $H1$	1561	169	1.10	23.6	23.59	⋯	⋯
Mayall/NEWFIRM $H2$	1707	176	1.06	23.6	23.61	⋯	⋯
Mayall/NEWFIRM K	2170	307	1.08	23.5	23.85	⋯	⋯
CFHT/WIRCAM J	1254	157	0.72	24.4	30.0	2MASS	Bielby et al. (2012)
CFHT/WIRCAM H	1636	287	0.68	24.5	30.0	⋯	⋯
CFHT/WIRCAM K_s	2159	326	0.65	24.3	30.0	⋯	⋯
HST/ACS F606W	596	231	0.12	28.8	26.491	USNOB1.0[d]	Koekemoer et al. (2011)
HST/ACS F814W	809	189	0.12	28.2	25.943	⋯	⋯
HST/WFC3 F125W	1250	301	0.19	27.6	26.250	⋯	⋯
HST/WFC3 F140W	1397	395	0.19	26.8	26.465	⋯	Skelton et al. (2014), Brammer et al. (2012)
HST/WFC3 F160W	1542	288	0.20	27.6	25.960	⋯	Koekemoer et al. (2011)
Spitzer/IRAC 3.6 μm	3563	744	1.80	23.9	21.581	2MASS	Ashby et al. (2015)
Spitzer/IRAC 4.5 μm	4511	1010	1.82	24.2	21.581	⋯	⋯
Spitzer/IRAC 5.8 μm	5759	1407	1.94	22.5	21.581	⋯	Barmby et al. (2008)
Spitzer/IRAC 8.0 μm	7959	2877	2.23	22.8	21.581	⋯	⋯

Notes.
[a] The 5σ depths correspond to $5\times$ the standard deviation of flux measurements in ∼5000 circular apertures, with a diameter of $2\times$ FWHM of the PSF, randomly placed across each image in the regions that are free of detected objects.
[b] Photometric zeropoint.
[c] The astrometric system was calibrated on the CFHTLS mosaics.
[d] This is the original astrometric system adopted for calibration in Lotz et al. (2008). See Section 3 for further details.

The astrometric calibration was based on the Naval Observatory Merged Astrometric Data set (NOMAD[35]), and was refined using the Sloan Digital Sky Survey (SDSS) DR7 catalog (Abazajian et al. 2009). The final internal and external astrometric uncertainties are 0.″02 and 0.″07, respectively (Gwyn 2012).

2.2.2. WIRCam Deep Survey

Deep broadband *J, H*, and *Ks* images from the WIRCam Deep Survey (WIRDS; Bielby et al. 2012) complement the *HST* WFC3 data. The images were obtained with the WIRCam instrument at the CFHT under good seeing conditions (FWHM ∼0.″6), and they cover 0.4 square degrees centered on the EGS. The 50% completeness limit for point sources ranges between 24.6 and 24.8 mag. The astrometry was calibrated using the Two Micron All Sky Survey (2MASS) catalog (Skrutskie et al. 2006) with a final internal accuracy of ∼0.″1 (Bielby et al. 2012).

2.2.3. NEWFIRM Medium Band Survey

The overlap of the CANDELS WFC3/F160W-band image with the mosaics of the NEWFIRM Medium Band Survey (NMBS, van Dokkum et al. 2009; Whitaker et al. 2011) amounts to ∼30% in the southeastern region of the CANDELS footprint (see Figure 2). The CANDELS EGS multi-wavelength catalog incorporates these data. The data were taken with the NEWFIRM camera mounted on the Mayall 4 m telescope at Kitt Peak. This NIR imaging survey used one traditional K_s filter and five medium-band filters in place of the usual *J* and *H* bands. Specifically, the *J* band was split into three filters *J*1, *J*2, and *J*3, and the *H* band was split into two filters, *H*1 and *H*2 (van Dokkum et al. 2009; see also Figure 1). The average seeing FWHM ranged from 1.″06 to 1.″16, and the photometric depth reaches AB = 23.5–24.4 mag (5σ in $2\times$ FWHM apertures), with a 50% point-source completeness at $K_s = 23.6$ mag. The NMBS mosaics were aligned to the CFHTLS i'-band images with an astrometric precision of ∼0.″1 over the entire field of view.

2.3. Spitzer

We also included the IR data from the *Spitzer* InfraRed Array Camera (IRAC; Fazio et al. 2004) for which the four bands center at 3.6, 4.5, 5.8, and 8.0 μm.

The 3.6 and 4.5 μm band mosaics were obtained by combining four different image sets, two from the cryogenic mission and two from the warm mission phases. The first cryogenic data imaged a narrow $2.^\circ3 \times 0.^\circ29$ strip overlapping with the AEGIS *HST*/ACS imaging (PID 8, Barmby et al. 2008). The depth and width of the central ∼1° portion were later increased (PID 41023, PI: Nandra), providing better overlap with the deep (800 ks) X-ray imaging by *Chandra*.

[35] http://www.nofs.navy.mil/nomad/

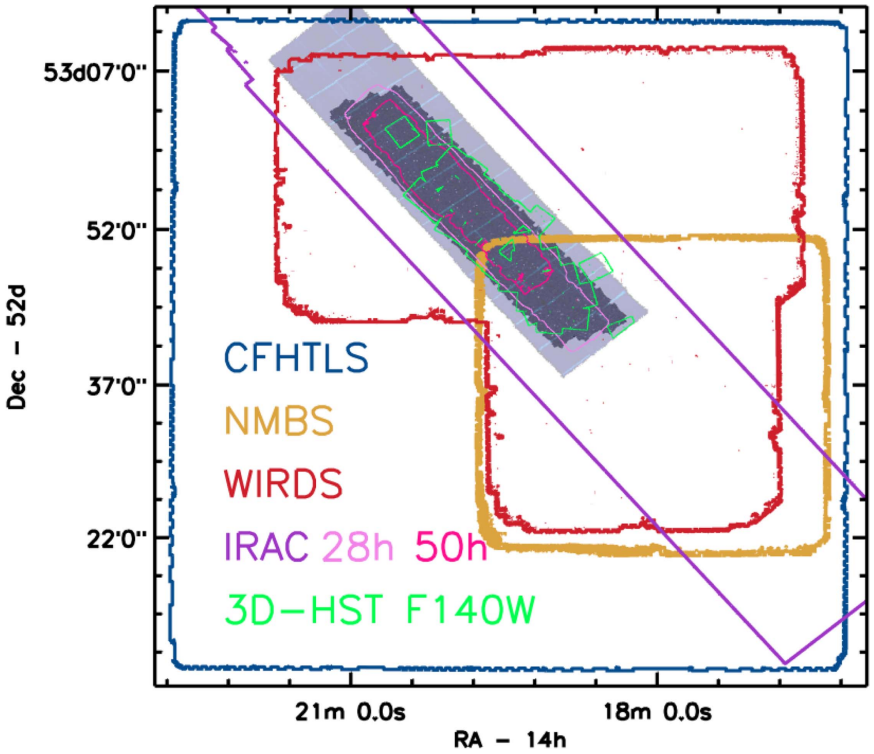

Figure 2. Coverage map of the different data sets used in this work. The dark filled area shows the coverage of the *HST* WFC3 F160W band from CANDELS, which has been adopted as the detection band. This area amounts to ∼200 arcmin^2. The light-blue filled region reproduces the ACS F606W exposure map from the AEGIS project (Davis et al. 2007), which fully covers the F160W map. The other data sets are also outlined: CFHTLS (optical broadband u^*-to-z', blue contour), WIRDS (Bielby et al. 2012; NIR *J*, *H*, and *Ks* bands, red contour), S-CANDELS (Ashby et al. 2015; dark purple: full coverage of the IRAC 3.6-to-8.0 μm mosaics; pink: 28 hr depth; magenta: 50 hr depth coverages), NMBS (Whitaker et al. 2011; yellow contour), and 3D-*HST* (Skelton et al. 2014; green contour).

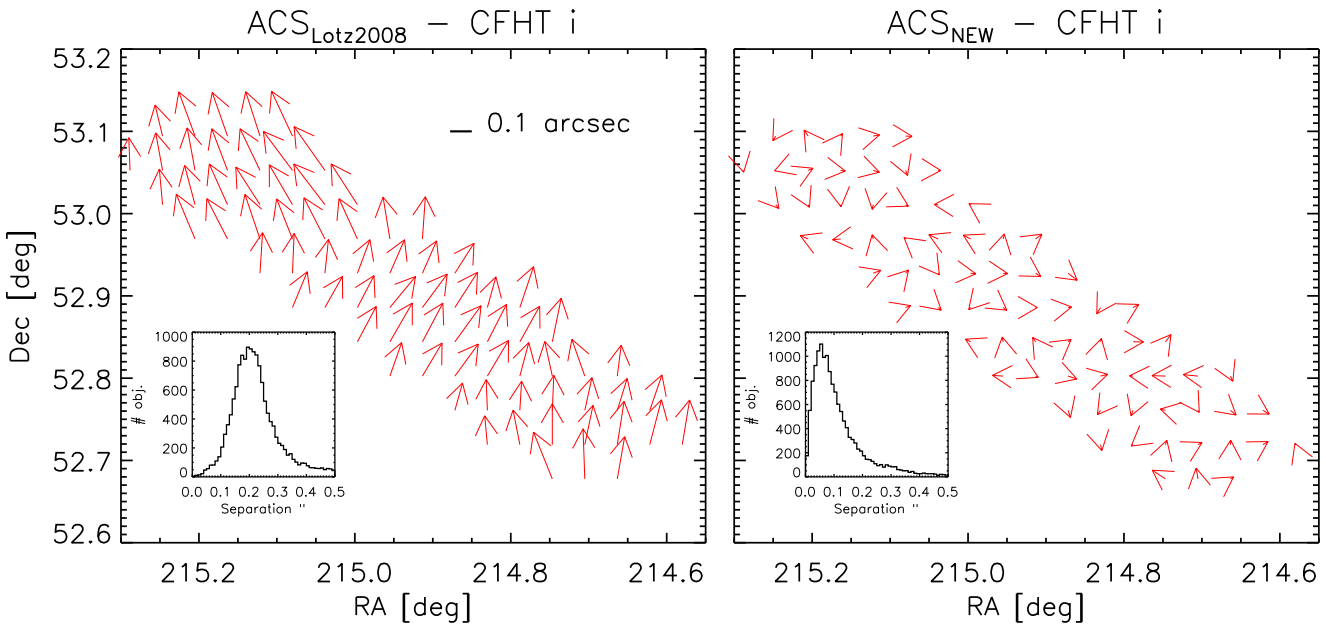

Figure 3. Left panel: offsets in R.A. and decl. positions between the previous CANDELS astrometric system (inherited from the AEGIS system) and the CFHTLS *i*-band system. Each arrow represents the average of the offsets measured from the matched objects within the rectangle region (1.′5 × 1.′5 in size) centered on the arrow tail. Right panel: similar to the left panel, but after correcting the CANDELS system to the CFHTLS system. The bands used for the recalibration are the ACS F814W and the CFHTLS *i* band. In both panels, the insets show the distribution of the offsets (bin size 0.″01): the median offset of the old astrometric calibration is 0.″2, while that of the offsets after applying the new astrometric solution is 0.″04.

These 3.6 and 4.5 μm data were combined with those from the warm mission phase, namely, those from the *Spitzer* xExtended Deep Survey (SEDS, PID 61042; Ashby et al. 2013) and *Spitzer*-CANDELS (S-CANDELS, PID 80216; Ashby et al. 2015). The resultant 3.6 and 4.5 μm mosaics cover most of the WFC3 F160W area to a depth of at least 50 hr and the rest to at least 28 hr in each band (see Figure 2; we refer to Ashby et al. 2015 for full details). The 5.8 and 8.0 μm mosaics,

on the other hand, were made from the cryogenic data of the AEGIS project (Barmby et al. 2008) and those of PID 41023 (PI Nandra). All these IRAC data were reprocessed and mosaicked using the same CANDELS *HST* tangent-plane projection and with a pixel scale of 0.″6/pixels, to prepare them appropriately for further photometric analysis (see also Ashby et al. 2015). The internal astrometry was checked by cross-matching approximately 500 point sources from the 2MASS catalog to the detections in the 3.6 and 4.5 μm mosaics. The 1σ dispersions in R.A. and decl. are $\lesssim$0.″2 in both bands.

2.4. Value-added Data

The CANDELS EGS field has a large number of spectroscopic redshifts and deep *Chandra* X-ray data. While they are not a part of the photometry, these data are included in our catalog (see Appendices A and C).

2.4.1. Spectroscopy

We included the spectroscopic redshifts from the DEEP2+3 Surveys (Coil et al. 2004; Willner et al. 2006; Cooper et al. 2011, 2012; Newman et al. 2013),[36] which were spectroscopic surveys targeting galaxies brighter than $R = 24.1$ mag. Observations were carried out using the DEIMOS spectrograph on Keck II with a resolution of $\lambda/\Delta\lambda \sim 5000$ at the central wavelength of 7800 Å. In the EGS field, the campaign covered a $\sim 30' \times 120'$ strip centered on the AEGIS ACS mosaic. Within the CANDELS F160W mosaic coverage, there are 2132 unique DEEP2+3 objects that have secure redshifts (quality parameter $Q \geqslant 3$) within a matching radius of 0.″8 (if more than one object falls within the matching radius, the closest match was adopted).

2.4.2. X-Ray Data

The EGS field was initially observed by *Chandra*/ACIS with a 200 ks integration time as part of the AEGIS project (AEGIS-X Wide, Nandra et al. 2005; Laird et al. 2009). The observations covered the full AEGIS ACS mosaic with eight pointings, $\sim 17' \times 17'$ each, for a total area of $\sim$0.7 deg^2. Recently, new *Chandra*/ACIS data to a nominal depth of 600 ks were acquired over a region of approximately 0.29 deg^2 centered on three central tiles of the AEGIS-X Wide coverage. These data have been combined with the previous 200 ks *Chandra*/ACIS observations to provide a cumulative depth of 800 ks in the three central ACIS fields (AEGIS-X Deep or AEGIS-XD, Nandra et al. 2015). The astrometry was calibrated using the CFHTLS *i*-band image as a reference (Nandra et al. 2015). The AEGIS-XD is currently the third deepest X-ray survey in existence, and it covers an area larger than the *Chandra* Deep Fields (CDFs) by a factor of three. While being approximately two to three times shallower than the CDFs, it is sufficient to probe the dust-obscured X-ray galaxy populations at high redshifts (e.g., $L_X \sim 10^{43}$ erg s^{-1} at $z \sim 3$ in the soft X-ray 0.5–2 keV band).

3. Astrometric Calibration of CANDELS *HST*/ACS and WFC3 Mosaics

The catalog is photometrically selected in the WFC3 F160W band and hence it inherits the astrometry of this image. The

[36] http://deep.ps.uci.edu/DR4/home.html and http://deep.ps.uci.edu/deep3/ for DEEP2 and DEEP3, respectively.

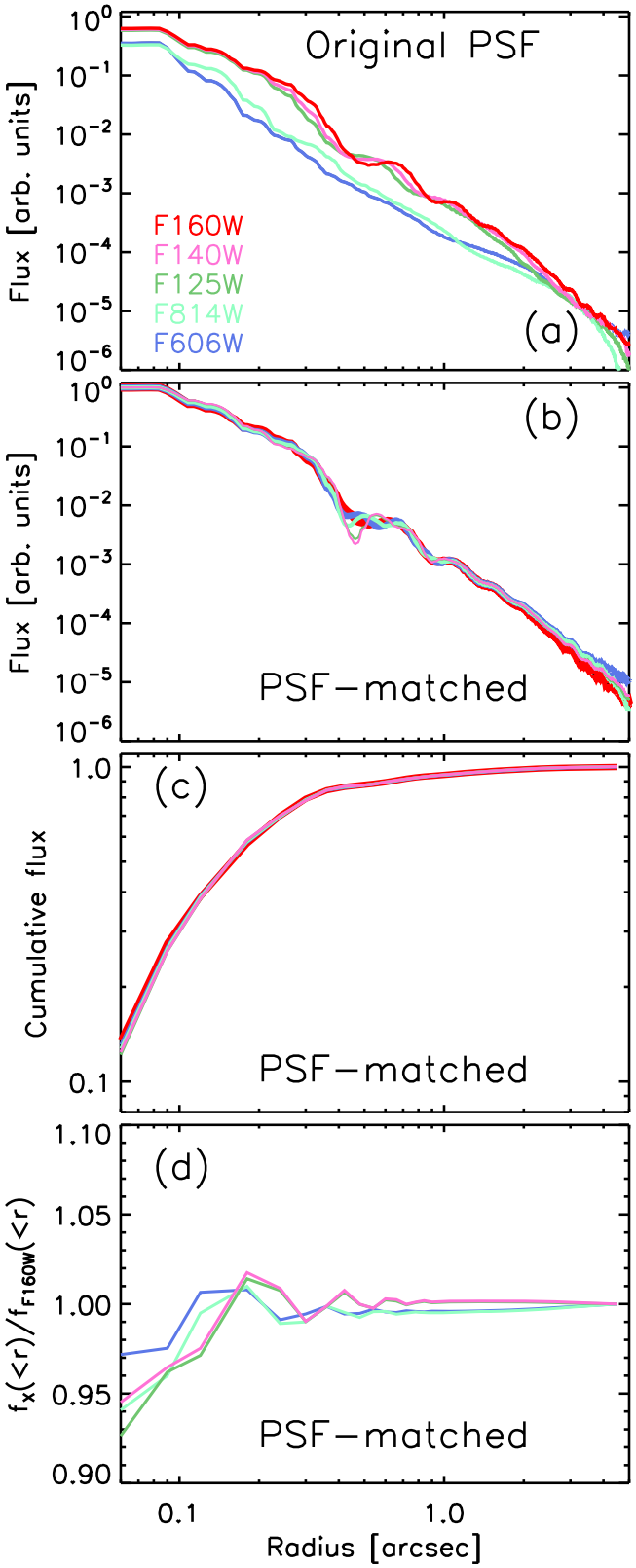

Figure 4. Top to bottom panels are as follows. (a) Original PSF profiles of the *HST*/ACS F606W, ACS F814W, WFC3 F125W WFC3 F140W, and WFC3 F160W bands. (b) Similar to the previous plot, but after PSF matching to F160W. (c) Growth curves in the same four bands after PSF matching. (d) Ratios of the cumulative flux in the four bands after the PSF-matching to that of F160W, shown as a function of radius. The color-coding scheme is the same in all panels.

Table 2
Main SExtractor Parameters in the Hot and Cold Modes

Parameter Name	Cold Mode	Hot Mode
DETECT_MINAREA	5.0	10.0
DETECT_THRESH	0.75	0.7
ANALYSIS_THRESH	5.0	0.7
FILTER_NAME	tophat_9.0_9x9.conv	Gauss_4.0_7x7.conv
DEBLEND_NTHRESH	16	64
DEBLEND_MINCONT	0.0001	0.001
BACK_SIZE	256	128
BACK_FILTERSIZE	9	5
BACKPHOTO_THICK	100	48.0

earlier astrometry of the CANDELS EGS WFC3 and ACS mosaics was calibrated using the AEGIS ACS catalog from Lotz et al. (2008). This calibration was based on the CFH12K mosaic of Coil et al. (2004), which was tied to the USNOB1.0 catalog. However, a comparison between the F160W positions using this earlier astrometric solution and the CFHTLS D3 i'-band positions revealed systematic offsets. Figure 3 presents the measured offsets. Both the amplitude and the direction of the offset vary across the field, with a median offset of $\sim 0\farcs2$, significant enough to cause potential problems in many applications. Indeed, previous works already showed that the median dispersion of the positions of a given object imaged on multiple overlapping plates in the USNOB1.0 catalog generated offsets up to $0\farcs2$–$0\farcs6$ in the position of extended objects compared to the SDSS Early Data Release (Stoughton et al. 2002—see Monet et al. 2003) or to PPMX (Roeser et al. 2010).

Because the CFHTLS D3 astrometry implements higher-quality data and a better calibration (in particular, the SDSS calibration), we believe that it is more trustworthy. For the sake of internal consistency, we have opted to keep the WFC3 and ACS mosaic images unchanged in this version of the data release and to register all the F160W source positions to the CFHTLS D3 system at the catalog level.

This astrometric registration was achieved as follows. At first, we matched the WCS coordinates of the objects in the ACS F814W catalog of Lotz et al. (2008) to those in the CFHTLS D3 catalog of Gwyn (2012). A matching radius of $\farcs5$ was adopted. The full region was then divided into contiguous tiles, each 1.5×1.5 arcmin^2 in size. This size was chosen as a compromise between obtaining a sufficient number ($\sim$100) of objects in each tile to reduce the statistical uncertainties and yet keeping the tiles as small as possible in order not to lose the resolution. In each tile, the average of the displacements between the F814W and the CFHTLS coordinates was computed. These averages were used as the input to the IRAF (Tody 1986, 1993) task geomap to generate the surface, which converts one astrometric system to the other. The task was run interactively, adopting a fifth-order Legendre function to represent the surface, as it turned out to provide the best results in terms of residuals. In this process, we rejected a few objects with residuals larger than 3σ. Finally, we re-registered the F814W coordinates to the new system by applying the best-fit surface to correct the positions.

After applying the correction, the astrometry shows much less discrepancy with respect to the CFHTLS D3 system, with a median offset of $\sim 0\farcs04$, i.e., a factor of $5\times$ smaller than the previous astrometric solution (see the right panel of Figure 3). This is in agreement with the average offsets of our catalogs in other CANDELS fields when compared to the external catalogs. Our final catalog adopts this new astrometric solution and the WCS positions in the catalog refer to this improved system. For backward compatibility, we also provide the positions using the earlier AEGIS ACS system (columns RA_LOTZ2008 and DEC_LOTZ2008 in the photometry catalog; see Appendix A). In the CANDELS repository, we provide for download the versions of the *HST*/ACS and WFC3 mosaics registered to the Lotz et al. (2008) and to the CFHTLS D3 system as well.

4. Photometry

For the flux measurements in the CANDELS EGS photometric catalog, we adopted two different approaches, depending on the angular resolution of the images, as parameterized by the FWHM of the PSF charactersic of each band. For the high-resolution images, i.e., all the *HST* bands, the photometry was performed using SExtractor (Bertin & Arnouts 1996) in dual-mode with a detection on the F160W band and measurements on the PSF-matched ACS/WFC3 images matched to the F160W resolution, the lowest in our *HST* data set. For the low-resolution images, i.e., all the ground-based data and the *Spitzer*/IRAC images, the photometry was performed using the TFIT software (Laidler et al. 2007), which uses a morphological template-fitting technique. These procedures have been extensively described by Galametz et al. (2013) and Guo et al. (2013).

4.1. PSF and Convolution Kernels

For the *HST* and IRAC bands, the empirical PSFs were constructed from a set of high S/Ns and isolated point sources using IRAF/DAOPHOT (Stetson 1987). Despite the fact that IRAC PSFs vary across the mosaics due to the heterogenous nature of the input data and the intrinsic variations in the instrument itself, we opted for a single IRAC PSF in each band. For the ground-based optical and NIR images, the PSFs were created by stacking a number (6–21) of bright and isolated point sources. The convolution kernels were obtained using the IRAF/lucy task, for later uses in either PSF-matching or TFIT. Figure 4 shows the light profile of the empirical *HST* PSFs before and after the PSF-matching process, together with the growth curves of the PSF-matched point sources. The growth curves do not show any significant offset with respect to that of the F160W band. Within the central 2 pixels ($0\farcs12$), the differences amount to $\sim$5%. By 8.3 pixels ($0\farcs5$) the differences essentially vanish.

4.2. Photometry of HST Images

Both source detection and photometry were performed using a modified version of SExtractor v2.8.6, which was already used in the construction of the CANDELS UDS (Galametz et al. 2013) and GOODS-S (Guo et al. 2013) catalogs. This modified version provides a better measurement of the local background by imposing a minimum inner radius of $1''$ for the sky annulus (see Grazian et al. 2006; Galametz et al. 2013) and refines the cleaning process by rejecting non-detections that are often merged to real sources (Galametz et al. 2013).

A single configuration of SExtractor usually does not provide the most optimal detection of all the objects in an image. Indeed, it is difficult to reach the balance that can achieve high completeness for faint objects without a large

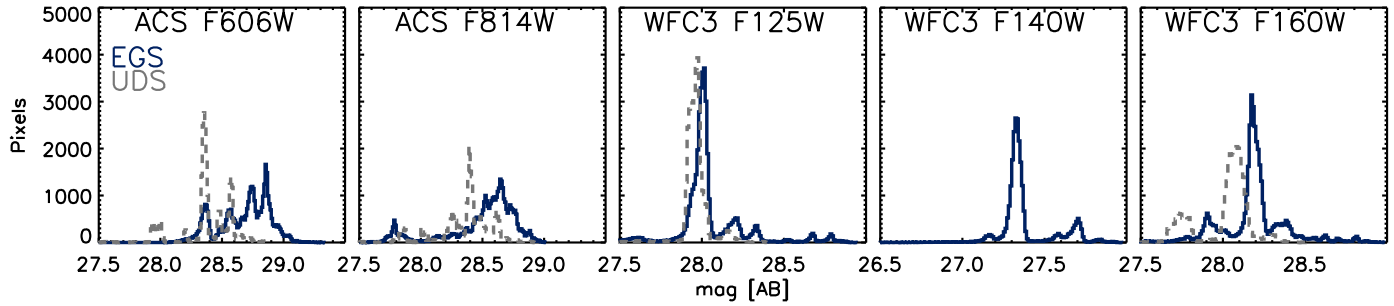

Figure 5. Distributions of the pixel-by-pixel 1σ magnitude limits in the five *HST* bands in the EGS (blue solid line) and the UDS (gray dashed line) fields. The UDS catalog does not include the F140W band from 3D-*HST*. The limits were calculated from the rms maps and are scaled to an area of 1 arcsec^2. The bin width is 0.01 mag for all bands.

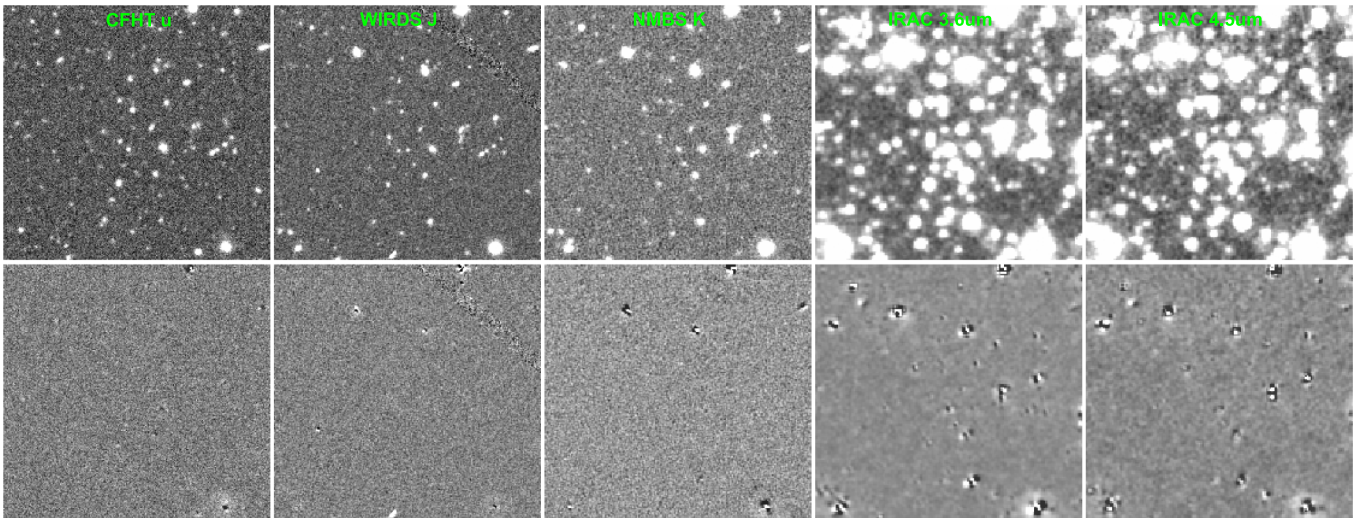

Figure 6. Examples of residuals after the second pass of TFIT. Cutouts $\sim 80'' \times 80''$ from the original science images are shown in the top row for CFHT u^*, WIRDS *J*, NMBS *K*, IRAC 3.6 μm, and IRAC 4.5 μm bands, respectively, from left to right. The corresponding cutouts of the residual images are shown in the bottom row.

number of spurious detections caused by oversplitting bright and/or extended objects. Therefore, we adopted the same two-step approach used for the CANDELS GOODS-S and CANDELS UDS fields (Galametz et al. 2013; Guo et al. 2013). First, SExtractor was run in the so-called cold mode: the relaxed values of the detection parameters allow for a reliable extraction and deblending of the brighter sources. In the second run, called the hot mode, the detection parameters were tuned to optimize the detection of faint and blended objects. Table 2 presents the main Sextractor parameter values adopted for the cold and hot mode (see Appendix A in Galametz et al. 2013 for the full list of SExtractor parameters). These two initial catalogs were then merged to keep the objects that are detected in at least one catalog. However, those objects in the hot catalog falling within the Kron (1980) ellipse of the cold-mode sources were rejected because these are likely the result of an excessive source shredding (see also, e.g., Caldwell et al. 2008; Gray et al. 2009; Barden et al. 2012).

The photometry in both the cold and the hot modes was performed in the dual-image mode of SExtractor, using the F160W band for the detection. As shown in Table 1, the FWHM of *HST* PSFs differ from band to band, and the F160W-band PSF has the widest FWHM. To ensure the most accurate color measurements, we used the IRAF/psfmatch task to homogenize the PSFs of the mosaics in the F606W, F814W, F125W, and F140W bands to the PSF of the F160W band. Figure 4 shows the profiles of the *HST* PSFs before and after the PSF-matching procedure. The after-matching ones deviate from the F160W PSF at only a few percentage levels, which validates our matching process.

Different flux measurements were derived. Specifically, fluxes were measured using Kron (1980) elliptical apertures (SExtractor FLUX_AUTO), isophotes (FLUX_ISO) and a set of 11 circular apertures (FLUX_APER). These individual values are reported in the supplemental catalogs that accompany our main catalog.

The flux measurement provided by SExtractor inside the Kron aperture is within 6% of the total flux (Bertin & Arnouts 1996), and it is thus often regarded as the measurement of total flux (but see, e.g., Labbé et al. 2003 and Graham & Driver 2005 for discussions on the deviation of SExtractor FLUX_AUTO from the total flux). However, this often is not ideal for a faint source in terms of S/N because the large aperture needed to capture the total flux necessarily includes noise from many background pixels, potentially swamping the signal from the targets. On the other hand, the isophotal flux that maximizes the S/N for faint sources could underestimate the total flux because of the smaller aperture in use. If the flux measurements of a given object in different bands are done through the same aperture (i.e., through the dual-image mode as we did here), the isophotal fluxes will give the best measurements of colors. This kind of measurement is crucial for most of the possible applications of our catalog such as SED fitting.

In our main catalog, the FLUX_AUTO values were adopted as the total flux measurements in the F160W band. In any other *HST* bands, the quoted total fluxes were derived through the flux ratio with respect to the F160W band in terms of FLUX_ISO, i.e.,

$$f_{\mathrm{tot},b} = f_{\mathrm{iso},b} \times \frac{f_{\mathrm{auto,F160W}}}{f_{\mathrm{iso,F160W}}} \quad (1)$$

where $f_{\mathrm{tot},b}$ and $f_{\mathrm{iso},b}$ are the total and isophotal flux for band b, respectively, while $f_{\mathrm{auto,F160W}}$ is the Kron-aperture flux in the F160W band. The area adopted for the measurement of the isophotal flux $f_{\mathrm{iso},b}$ is defined from the F160W mosaic and it is thus the same for all bands. $f_{\mathrm{tot},b}$ is therefore a Kron-like flux measurement recovered from the higher S/N isophotal flux estimate. The validity of Equation (1) relies on the fact that the morphologies of the galaxies in our catalog do not vary with wavelength. Indeed, the majority of sources in our catalog have small sizes; furthermore, the smoothing introduced by the PSF-matching to the F160W-band resolution further acts in the direction of homogenizing the morphology of each source across the different bands. Similar approaches have been widely adopted in the literature (e.g., Whitaker et al. 2011; Galametz et al. 2013; Guo et al. 2013; Muzzin et al. 2013; Skelton et al. 2014). In particular, van de Sande et al. (2013) showed that stellar masses from Whitaker et al. (2011) are consistent with dynamical mass measurements recovered from absorption lines, increasing the confidence on physical parameter estimates from total flux measurements based on Equation (1).

Figure 5 presents the distribution of the 1σ depth in each *HST* band. The limiting magnitudes in the WFC3 bands roughly follow a tri-modal distribution, which is due to the different degrees of tile overlapping within the mosaics: the heavily overlapped regions among adjacent tiles have higher sensitivities than what is typical, while the boundary regions of less coverage have lower sensitivities. The distribution for ACS limiting magnitudes is broader and more complex than that of the WFC3 ones. One possible explanation for this is that the ACS mosaics are the result of two different data sets being combined together (AEGIS and CANDELS), each one likely with its own tri-modal distribution. Another possible explanation could be the different native pixel scale of the ACS camera compared to WFC3. The smaller pixel scale of ACS compared to WFC3 would result in lower S/Ns for each pixel (for the same cumulative S/N), introducing the uncertainty. Overall, the depths corresponding to the peak of the distributions in 1σ magnitudes reported in Figure 5 for each band are generally within $\approx$0.1 mag from the rescaled 5σ depths presented in Table 1 (obtained from randomly placed circular apertures), supporting our rms maps generation. Finally, the plots show that the average depth of the EGS *HST* mosaics is slightly deeper than that of UDS.

4.3. Photometry of Low-resolution Bands

4.3.1. TFIT Flux Measurement

The flux measurements for the low-resolution bands in the CANDELS multi-wavelength catalogs are based on TFIT (Laidler et al. 2007). A detailed description of this software is provided by Fernández-Soto et al. (1999), Papovich et al. (2001), and Laidler et al. (2007), while Lee et al. (2012) presented a set of simulations aimed at validating this template-fitting technique and quantifying its uncertainties. Briefly, the brightness profile of the source in the high-resolution image, identified from the segmentation maps, is convolved with the kernel required to match the low-resolution image PSF. The result is a template of the object in the low-resolution image. Its total flux can then be obtained via best fit. In this way, it is possible to use all the information from the high-resolution image to deblend the objects in the low-resolution bands. This procedure assumes that the morphology of each object does not depend on the wavelength. A wavelength-dependent morphology could result in the outer regions of some objects being excluded from their segmentation map. Furthermore, the outskirts of fainter and/or smaller objects could fall below the detection threshold and hence be missing from the segmentation map generated during the detection stage. In order to limit the potential loss of flux due to these effects, the area associated with each object in the segmentation map was expanded following the empirical relation of Galametz et al. (2013). The fluxes measured by TFIT have been proven to be very close to total fluxes (Lee et al. 2012), and hence no further aperture correction was applied to them.

Template-fitting techniques require good alignment between the high-resolution and the low-resolution images. However, the astrometric calibration of the low-resolution images could be different from that of the high-resolution one in the method and/or the reference catalog, which could result in slight offsets in alignment. Furthermore, geometric distortions, if not perfectly corrected, could also produce local misalignments among images. All this could result in catastrophic failures in template fitting. To overcome this problem, TFIT also measures small position offsets between the high- and low-resolution images. TFIT is then run for a second time, using this information as part of the input to adjust the alignment locally by allowing a slight freedom of the centroid during the fitting process. Figure 6 presents an example of the second-pass residual images of a small section in the EGS field. The clean residual images indicate that the fitting procedure was successful.

4.3.2. Background Assessment

A key factor in reliable flux measurement is the determination of the background. TFIT does not attempt any measurement of the background, but instead assumes a zero-background everywhere in the mosaic. Therefore, the background must be subtracted in advance. The full procedure of background estimate and subtraction for the CANDELS multi-wavelength catalog construction was described by Galametz et al. (2013).

We assessed the goodness of our background subtraction by measuring the fluxes and the associated uncertainties in about 10^4 empty apertures (i.e., placed at locations free of known sources) across the residual images created by TFIT after subtracting off all the sources detected in F160W. The statistical distribution of the ratio between the flux measurements and their associated uncertainties should then be described by a standard normal distribution (i.e., zero mean and unit standard deviation). We performed the flux measurements adopting three different aperture values ($0\farcs5$, $1\farcs0$, and $2\farcs0$). Figure 7 shows the distribution of the S/N measurements for the ground-based data.

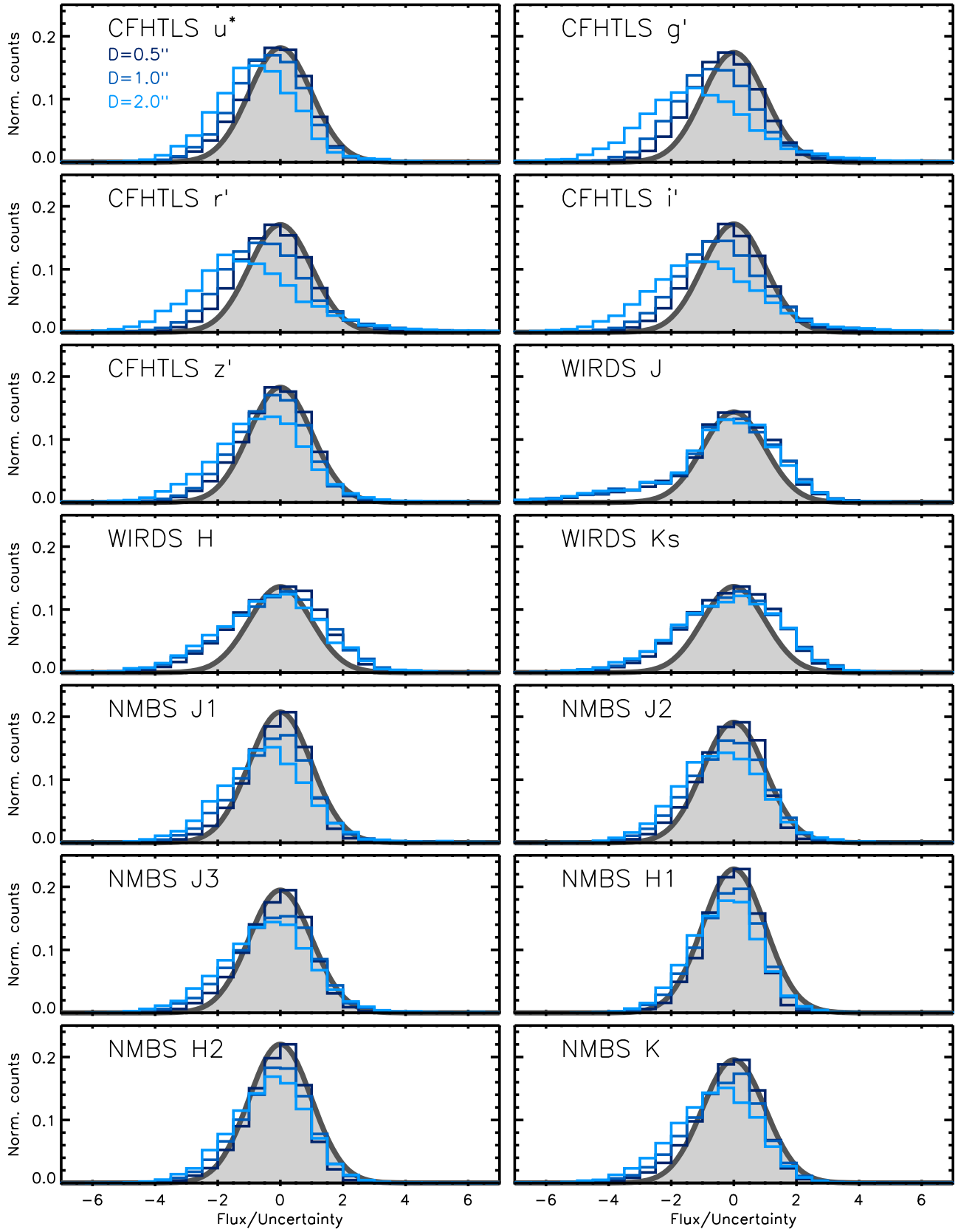

Figure 7. Histograms showing the background level in units of the local noise level, for the background-subtracted ground-based bands. The bin width is 0.5. The noise value was computed from the rms maps. The three different blue shades refer to empty apertures randomly positioned on the residual map avoiding any already detected source and adopting three different apertures: $0\farcs5$, $1\farcs0$, and $2\farcs0$, as indicated by the legend. These histograms have been renormalized to the total number of used apertures ($\sim 10^4$). For reference, we also plot as a gray curve a standard normal distribution, whose peak value has been normalized to that of the $D = 0\farcs5$ distribution. Most of the distributions are centered on S/N $\sim$ 0, and they are all consistent with zero at a 3σ level, validating the background correction procedure. We relied on `SExtractor` background measurement capabilities for the *HST* bands.

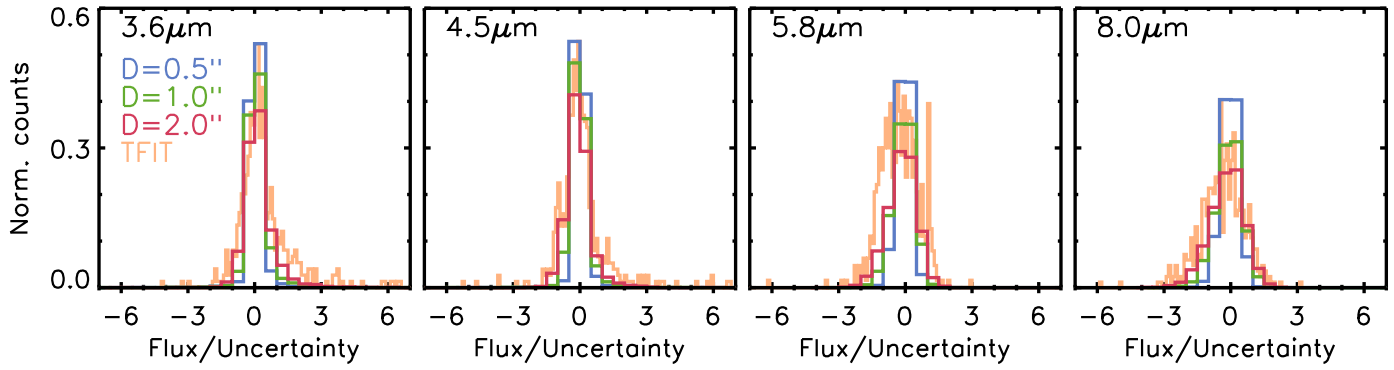

Figure 8. Histograms showing the background level in units of the local noise level, for the background-subtracted ground-based bands. The orange histograms present the data from the TFIT recovery of the simulated sources, while the blue, green, and red ones refer to the apertures as indicated by the legend (see Section 4.3 for more details). These histograms have been renormalized to the total number of used apertures. The distributions are centered on zero, which further validate our background subtraction procedure.

The distributions very closely match the standard normal distribution, as expected.

Since the background subtraction in the IRAC bands is even more challenging, for these bands, we complemented the above test with a Monte Carlo simulation as follows. A set of 500 positions were randomly chosen in regions free of any objects detected in the F160W band. We simulated the presence of the objects by adding these 500 positions to the input catalog for TFIT. Because TFIT needs to refer to the segmentation map for the shape information, we also simulated exponential and de Vaucouleurs (1948) profiles through the `IRAF mkobject` task and added their footprints to the segmentation map. The science mosaics were not altered. The simulated objects have circularized effective radii uniformly distributed between $0\farcs6$ and $2\farcs4$ (after taking into account the PSF), which fully encompass the distribution of apparent sizes of the objects detected in the WFC3 F160W mosaic. `TFIT` was then re-run with this new catalog, adopting the same configuration used for the actual photometry, with the noise values computed from the rms maps. The forced flux measurements at the positions of the simulated sources, which are not actually present on the science mosaics, should statistically be zero.

The results from this test, in terms of S/N distribution, are shown in Figure 8 together with the S/N from the empty aperture measurements. Most of the distributions are centered on S/N ~ 0, and they are all consistent with zero at the 3σ level, validating the background correction procedure. We relied on `SExtractor` background measurement capabilities for the *HST* bands.

4.4. Multi-wavelength Photometric Catalog Creation

Flux measurements from the PSF-matched bands and from the `TFIT` process were finally merged together to produce the final catalog. This step was trivial because each object kept its unique ID throughout all the processes, and therefore the matching was done based on the ID rather than on the coordinates.

The final catalog includes photometry in 22 bands for 41,457 objects detected to a depth of 27.6 mag (5σ) in F160W. For each object, the catalog contains the flux measurement and the associated uncertainty. The catalog includes two distinct measurements for the IRAC 5.8 and 8.0 μm bands. One was obtained with an older kernel and was used for the computation of photometric redshifts and stellar masses. The second measurement was obtained with an improved kernel (see Appendix A). The plots presented in this paper refer to the improved kernel version of the IRAC 5.8 and 8.0 μm photometry. The catalog also includes all the objects with reliable (quality flag $Q \geqslant 3$) spectroscopic redshifts from DEEP2+3 (Coil et al. 2004; Cooper et al. 2011, 2012; Newman et al. 2013).

A flag mask, built from the F160W science mosaic, weight, and rms maps, is included with the catalog in this data release to indicate whether the object is very close to a bright star, falls within a defect region such as the teardrops (circular regions of dead pixels in the WFC3 array, $\sim$50 pixels in diameter), or is in a location of higher noise than usual. Figure 9 shows an example of mask for a bright star and an example of a teardrop. Details on how the flag mask was generated are given in Appendix B of Galametz et al. (2013).

The EGS field is at Galactic latitude $b \sim 60°$; therefore, the Galactic foreground extinction is expected to be minimal. Furthermore, the region of sky covered by the EGS footprint is small compared to the characteristic scale over which the Galactic foreground extinction varies, hence a single value for the Galactic foreground extinction in each band for all the objects in the catalog should suffice. Considering also that the exact value of the extinction in each band depends on the adopted dust model (e.g., for EGS $A_V = 0.025$ mag for a Cardelli et al. 1989 model or $A_V = 0.022$ mag for a Fitzpatrick 1999 model), we opted not to apply any Galactic foreground extinction correction.

The main multi-wavelength photometric catalog is accompanied by three additional catalogs containing estimates of the weight, based on the median exposure time inside the segmentation map, an estimate of the limiting magnitude, obtained from the median of the values in the rms maps from those pixels inside the segmentation map and a number of morphological and photometric quantities recovered from `SExtractor` on a per-object basis. We refer the reader to the README file for full details on the content of each of these catalogs. Together with the multi-wavelength photometric catalog, with this work, we also release the catalogs of photometric redshifts, stellar masses, and physical parameters for all the detected objects, derived following the procedures of Dahlen et al. (2013) and Mobasher et al. (2015). Appendices A through D detail the content of each catalog. Two companion papers will present the rest-frame luminosities (D. Kocevski et al. 2016, in preparation) and the probability distribution

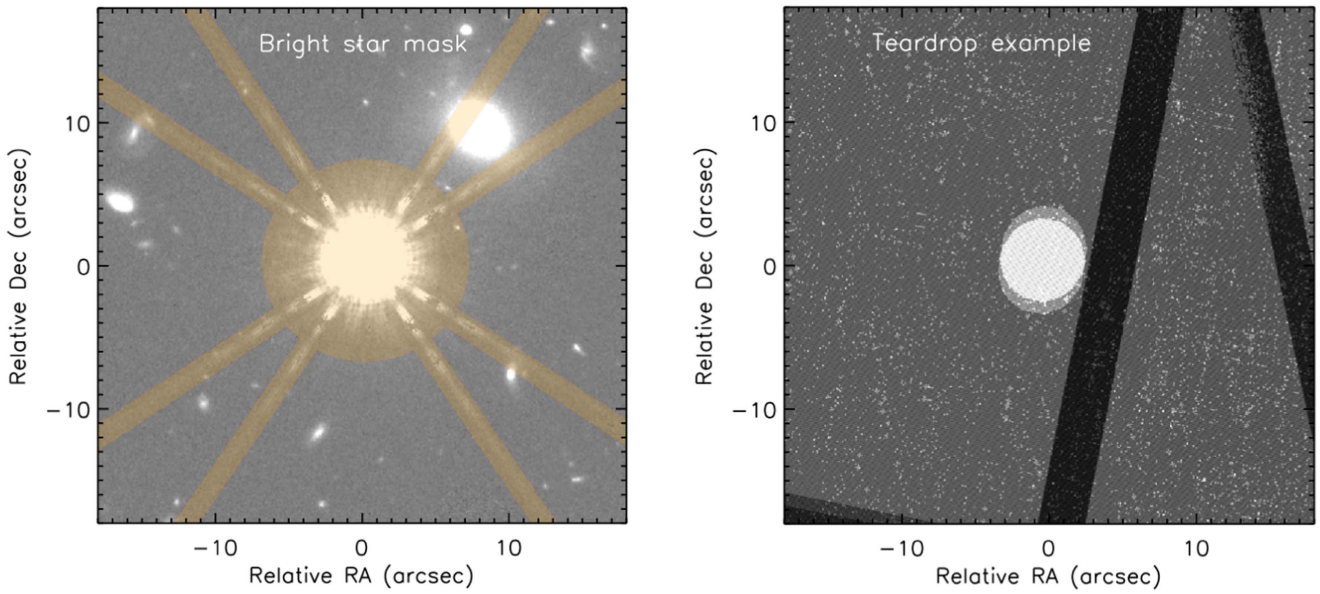

Figure 9. Left panel: example of the mask adopted for brights stars and their spikes. The gray-scale image shows the cutout of the WFC3/F160W mosaic centered on a bright star arbitrarily picked from the photometric catalog. The yellow area marks the region set in the flag map to enclose the bright star and its spikes because these could either contaminate the photometry and/or generate spurious detections. Right panel: example of a teardrop. The figure shows the cutout of the rms map associated to the WFC3/F160W mosaic, centered on a region of higher rms signal (a teardrop, the white spot in the center). Regions like the one shown have also been detected and masked. The darker regions correspond to lower rms values from the overlap of contiguous exposures.

functions of photometric redshifts (D. Kodra et al. 2016, in preparation).

For the CANDELS EGS multi-wavelength catalog, we also matched the positions of objects detected in the F160W mosaic to the objects detected in the *Chandra* 800 ks maps of Nandra et al. (2015). The most reliable counterparts to the X-ray sources were identified using a maximum-likelihood technique using the redder and deeper bands available (see Nandra et al. 2015 for details). The matching procedure resulted in 246 objects of the F160W-based-multi-wavelength catalog being likely X-ray emitters.

5. Assessment of Catalog Properties

In the following subsections, we present the tests that we performed to check the consistency of the photometry. These tests consist of both comparisons to external catalogs and of the assessments of the internal self-consistency.

5.1. Detection Completeness

The assessment of the completeness of sources in a catalog is a complex task, which ultimately depends on the class of objects considered and on the specific physical property under analysis. In this subsection, we estimate the completeness in the detection of sources, while in Section 6.4, we show an example of the completeness assessment in stellar mass.

We evaluated the detection completeness for both point and extended sources. For point sources, 100 PSFs randomly distributed across the whole field were added to the detection image without any restriction on their positions, and then we detected them using the same `SExtractor` configuration (two passes) adopted in the actual photometry. The process was repeated 20 times in each magnitude bin (width 0.25 mag) to increase the statistical significance. Although the above procedure provides robust completeness measurements for point sources, to allow for a more direct comparison with completeness measurements from other surveys, the procedure was repeated, excluding from the possible random positions those regions of the image that were already occupied by other sources, as identified by the segmentation map. This second method provides a strict upper limit on the completeness measurement. The two curves are presented in the left panel of Figure 10. The curve corresponding to the detection completeness recovered ignoring any restriction on object position (i.e., the *no-segmap* case) shows lower completeness values than those obtained excluding already detected sources (*segmap* case) for most of the magnitude range. This difference highlights the impact of source confusion. The 90% and 50% completeness limits for point sources are F160W = 26.62 mag and 27.18 mag, respectively, when the random positions are not checked against the segmentation map. Excluding from the simulation the position of all the detected objects, the limits are F160W = 26.91 mag and 27.23 mag, respectively.

The completeness for extended sources is sensitive to two main factors. (1) Compared to a point source of the same total flux, an extended source suffers from higher background noise because the extraction area must be larger, which results in a lower S/N. This means that the S/N of extended objects falls below the detection threshold at a brighter total flux level as compared to that of point sources, resulting in a lower completeness for extended sources. (2) Extended objects are more prone to the source blending problem, and hence the difficulty to properly deblend sources causes a further decrease of completeness.

In order to better model the effect of extended sources in the completeness estimate, the completeness for extended sources was computed adopting two different brightness profiles: an exponential disk (i.e., Sérsic index $n = 1$), typical of disky galaxies, and a de Vaucouleurs (1948) profile (Sérsic index $n = 4$), which characterizes elliptical galaxies. For each profile, a grid in apparent magnitude and circularized effective radius was constructed. Successively, using the `IRAF mkobject`

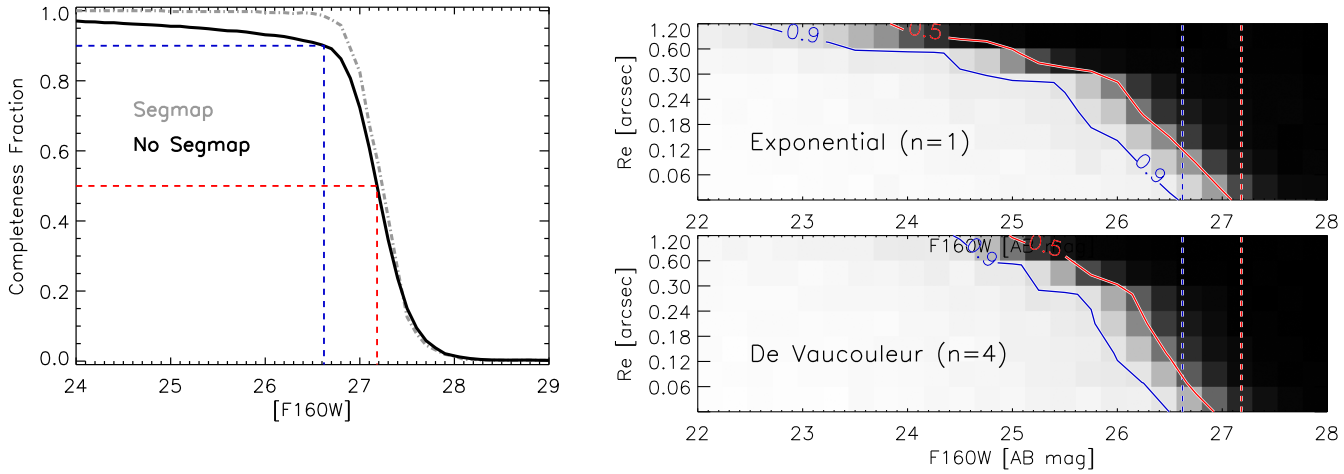

Figure 10. Detection completeness. The left panel shows the detection completeness on the CANDELS F160W image for a point source, obtained from a Monte Carlo simulation. The dotted–dashed gray curve is calculated masking all the already detected sources, while the solid black curve is calculated keeping all of the sources. The blue and red dashed lines indicate the 90% and 50% completeness levels and corresponding magnitudes. The two panels on the right show the completeness for extended objects, for the two cases of an exponential (top panel) and a De Vaucouleur profile (bottom panel) with circularized effective radii in the range of 0.″06–1.″2, obtained from a Monte Carlo simulation. The solid red and blue curves mark the 50% and 90% completeness limits, while the vertical red and blue dashed lines represent the 50% and 90% completeness limits from the point-source completeness simulation.

task, 100 galaxies with morphological properties drawn from the grid were added to the science image at random places across the image with no constraints on their position,[37] and photometry was performed with SExctractor. The process was repeated 10 times to increase the statistical significance. The results are shown in the panels on the right side of Figure 10. The 90% completeness limits for the exponential and the de Vaucoulers profiles for $R_e = 0.''3$ (roughly corresponding to the median value of R_e of the objects in the catalog with F160W brighter than 26.5 mag; the R_e of objects with magnitudes fainter than this value become close to those of point sources) is 25.40 mag and 25.62 mag respectively.

As expected, the completeness limits for point sources reach fainter magnitudes than the corresponding limits for extended objects. Furthermore, objects with disky morphologies ($n \sim 1$) and larger effective radii ($R_e \gtrsim 0.''3$) tend to be missed by the detection algorithm at brighter apparent magnitudes than objects with a more pronounced bulge (i.e., $n \sim 4$). For $R_e \lesssim 0.''3$ the detection completeness curves on the R_e-F160W plane, however, roughly coincide. This is not unexpected, since less extended and/or more compact sources are less sensitive to the differences in the observed (i.e., PSF-convolved) light profile.

5.2. Number Counts

The distribution of detected objects as a function of their apparent flux densities, the source number counts, is one of the most basic tests for the assessment of a sensitivity-limited catalog. The WFC3 F160W band number counts of our EGS catalog are presented in Figure 11.

For magnitudes brighter than ∼25 mag (which roughly corresponds to the completeness limit for our catalog when extended objects are taken into account), the number counts can be fitted by a power law with slope $\gamma = 0.700 \pm 0.006$. However, a better description of the data can be obtained by considering two power laws: one in the range of 17 mag $\lesssim$ F160W $\lesssim$ 20 mag and a second for 20 mag $\lesssim$ F160W $\lesssim$ 25 mag. In this case, the measured slopes are $\gamma = 0.89 \pm 0.08$ and $\gamma = 0.668 \pm 0.008$, for the brighter and fainter regimes, respectively. This double power-law behavior is qualitatively consistent with double power laws from previous analyses of number counts in NIR bands (see, e.g., Gardner et al. 1993; Ashby et al. 2015).

In the right panel of Figure 11, we compare our measurements to three recent F160W number count measurements from the literature, namely, the 3D-*HST* team's measurement of the EGS data (Skelton et al. 2014), the CANDELS UDS field (Galametz et al. 2013), and the CANDELS GOODS-S (Guo et al. 2013). All the measurements are consistent at least up to F160W ∼ 24 mag. The number counts from the UDS field are consistent with the EGS ones up to F160W ∼ 26.5 mag. In the range of 24 mag < F160W < 26.5 mag the GOODS-S number counts are below the UDS and EGS measurements by a factor of up to 1.2 at F160W = 26 mag, which could be due to the slightly shallower depth (0.2 mag) of GOODS-S compared to EGS. The number counts from 3D-*HST* agree completely with the measurements from the CANDELS EGS catalog of up to F160W ∼ 24 mag, while at 24 mag < F160W < 26.5 mag they show an excess with respect to those from the CANDELS UDS and the CANDELS EGS up to a factor of ∼1.2 at F160W ∼ 26 mag. One possible explanation for this excess could be that the detection for the 3D-*HST* catalog was performed on the noise-equalized combination of WFC3 F125W, F140W, and F160W bands, which could help in the detection of fainter sources. At magnitudes fainter than F160W ∼ 26.5 mag, we observe an abrupt decay in the number counts in all three catalogs, which is likely a consequence of the completeness for extended sources in the F160W band (adopted for the source detection).

5.3. Color–Color Plots

Figure 12 presents six color–color diagrams. We selected stars to be those objects with `SExtractor CLASS_STAR`

[37] The uniform distribution of random positions still neglects the clustering of galaxies and thus provides an upper limit to the completeness. However, given the low number of added sources compared to the total number of objects in the catalog, the completeness recovered in this way should still reflect a reliable estimate of the completeness for extended sources.

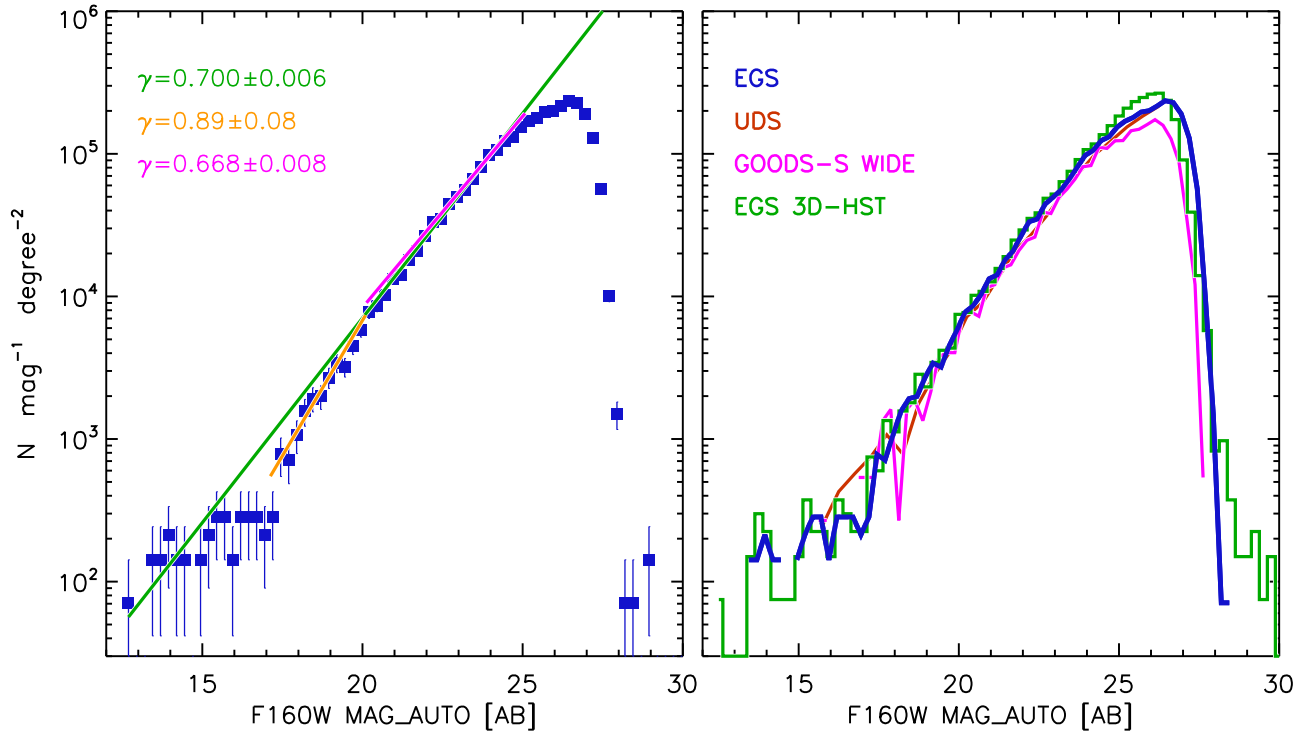

Figure 11. Left panel: number counts based on the detection in the WFC3 F160W band for CANDELS EGS (filled blue squares with poisson error bars). The green, magenta, and yellow lines represent the best-fitting power law over the ranges of 17 mag $\lesssim$ F160W $\lesssim$ 25 mag, 17 mag $\lesssim$ F160W $\lesssim$ 20 mag, and 20 mag $\lesssim$ F160W $\lesssim$ 25 mag, respectively. The measured power-law slopes are also indicated by the legend. Right panel: the CANDELS EGS number counts are compared to other measurements from the literature: CANDELS UDS (solid brown line), CANDELS GOODS-S (solid magenta line), and 3D-*HST* EGS (green histogram). The four measurements are barely distinguishable from each other for 19 mag $\lesssim$ F160W $\lesssim$ 24 mag. The decrease in number counts starts at ≈24.7 mag, while at F160W $\sim$ 26.5 mag, we observe an abrupt decay in number counts, which is consistent with measurements from the other studies, and is likely a consequence of the detection image completeness for extended objects.

>0.9 and satisfying the following color–color criteria:

$$[z' - 3.6\ \mu\mathrm{m}] < 0.73 \times [g' - z'] - 1.8 \text{ for } [g' - z'] \leqslant 1.5 \quad (2)$$

$$[z' - 3.6\ \mu\mathrm{m}] < 0.40 \times [g' - z'] - 1.3 \text{ for } [g' - z'] > 1.5. \quad (3)$$

Most of the point sources occupy a well-constrained region across the plots, which should correspond to the stellar locus. We compared the stellar locus to the synthetic colors of stars from stellar synthesis models. Following what has been done for the CANDELS GOODS-S multi-wavelength catalog (Guo et al. 2013), and considering that the stars in the EGS field should mainly be the halo population (due to its high latitude of $b \sim 60°$) and thus should be metal-poor, we adopted a set of stellar models of low metallicities ([M/H] = −0.5) from the BaSeL stellar synthesis models (Lejeune et al. 1997, 1998; Westera et al. 2002). All the plots show a good agreement between the observed colors of point sources with the colors from the synthetic library. Figure 13 shows a color–color diagram built with IRAC fluxes with an S/N > 5 in all four IRAC bands. The point sources (most of them are likely stars) have approximately zero color in the Vega system, consistent with models of stellar atmospheres. The selection box from Stern et al. (2005) identifies AGNs for which SEDs can be largely represented by a power law (Donley et al. 2012); the X-ray sources constitute the majority of the objects inside the selection box, supporting our color measurements. The X-ray sources outside the selection box are likely AGNs for which the host galaxy outshines the active nucleus.

5.4. Comparison with Publicly Available Catalogs

A number of multi-wavelength photometric catalogs have been produced in the EGS field, (Bundy et al. 2006; Ilbert et al. 2006; Barro et al. 2011a; Whitaker et al. 2011 and Skelton et al. 2014). This section compares the CANDELS multi-wavelength photometry to the three publicly available catalogs that have a broad wavelength coverage and include the IRAC bands. Specifically, we consider the catalogs from the 3D-*HST* survey (Skelton et al. 2014), the catalog from the NMBS (Whitaker et al. 2011), and the catalog presented by Barro et al. (2011a). The comparison is done on a per-filter basis. Figure 14 shows the comparison of the CANDELS EGS photometry to that directly available from the public catalogs. However, as we explain in Section 5.4.1, the total fluxes for the 3D-*HST* and NMBS catalogs were the result of a number of corrections (e.g., zeropoint offsets, Galactic extinction, curve-of-growth). For this reason, Figure 15 presents a comparison after removing those corrections, because this should provide flux measurements as they were originally recovered from the mosaics.

5.4.1. 3D-HST

The 3D-*HST* multi-wavelength photometric catalog is described by Skelton et al. (2014). For the *HST* data, the measurements were done using `SExtractor` on the mosaics PSF-matched to the F160W band. The measurements for the ground-based data and the *Spitzer* data were done by using `MOPHONGO` (Labbé et al. 2005, 2006, 2013), a procedure similar to TFIT but with the difference that the photometry is

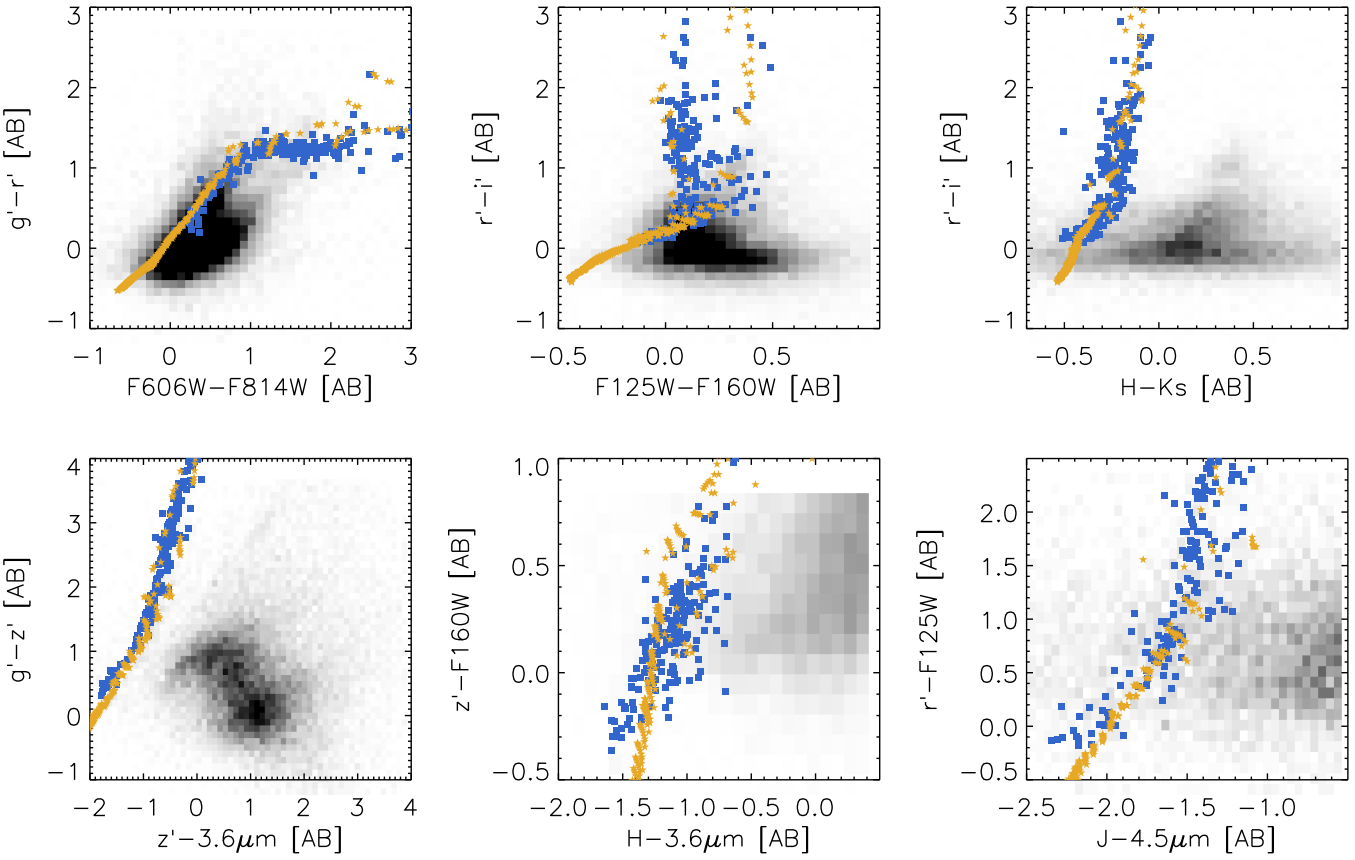

Figure 12. Color–Color diagrams. Objects brighter than F160W = 26.5 mag in the EGS catalog are presented as a gray-scale density plot, with darker color marking denser regions. Objects brighter than F160W = 22 mag and considered to be stars are marked by filled blue squares (see the main text for details). The yellow stars mark the colors of the model stars based on the BaSeL library, which have [M/H] = −0.5 and are typical of the Galactic halo stars.

done with a circular aperture after the target source is cleaned of its neighbors.

The measured fluxes of Skelton et al. (2014) were subject to a number of corrections with the aim of providing accurate measurements of the total flux. Based on Labbé et al. (2003; see, e.g., their Figure 5) the SExtractor FLUX_AUTO flux for faint sources can be systematically lower than the intrinsic total flux. Skelton et al. (2014) derived the offset between the two (i.e., the aperture correction) from the growth curve constructed from bright point sources, and calculated the fraction of the light enclosed by the circular aperture that has the same area as the Kron ellipse used in determining FLUX_AUTO. The measurement of the total flux in the F160W band was then obtained by applying the corresponding aperture correction to the FLUX_AUTO. Becuase the size of the Kron ellipse depends on the flux and is smaller for a fainter source, the applied correction depends on the source brightness as well, and it is larger for a fainter source. Total fluxes for the other bands were recovered as

$$f_{\mathrm{tot},b} = f_{\mathrm{ap},b} \times \frac{f_{\mathrm{tot,F160W}}}{f_{\mathrm{ap,F160W}}}$$

where $f_{\mathrm{tot},b}$ and $f_{\mathrm{ap},b}$ are the total and aperture flux for band b, respectively, while $f_{\mathrm{tot,F160W}}$ is the total flux in the F160W band. UV-to-K-band fluxes were corrected for the Galactic extinction following the extinction law of Cardelli et al. (1989; see Table 4 in Skelton et al. 2014). Finally, in Skelton et al. (2014) the photometric zeropoints were iteratively adjusted by computing the differences between the measured fluxes and the expected ones from the best-fit galaxy SEDs; the applied zeropoint offsets ranged from −0.22 mag in the u^* band to +0.17 mag in the NMBS/$J1$ band, though for 16 out of the 22 bands the zeropoint corrections are within 0.05 mag.

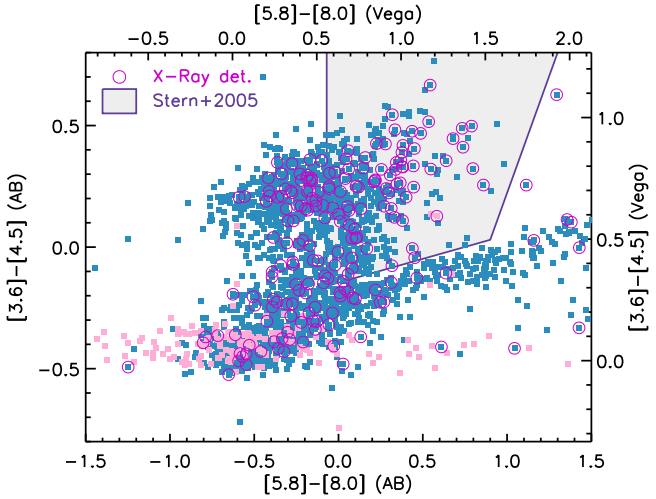

Figure 13. IRAC color–color plot. The blue points represent sources in the catalog with S/N > 5 in all four IRAC bands, while the pink points mark objects with CLASS_STAR > 0.95 and F160W < 22 mag. The shaded region marks the AGN selection box defined by Stern et al. (2005); magenta open circles identify those objects with detection in the X-rays.

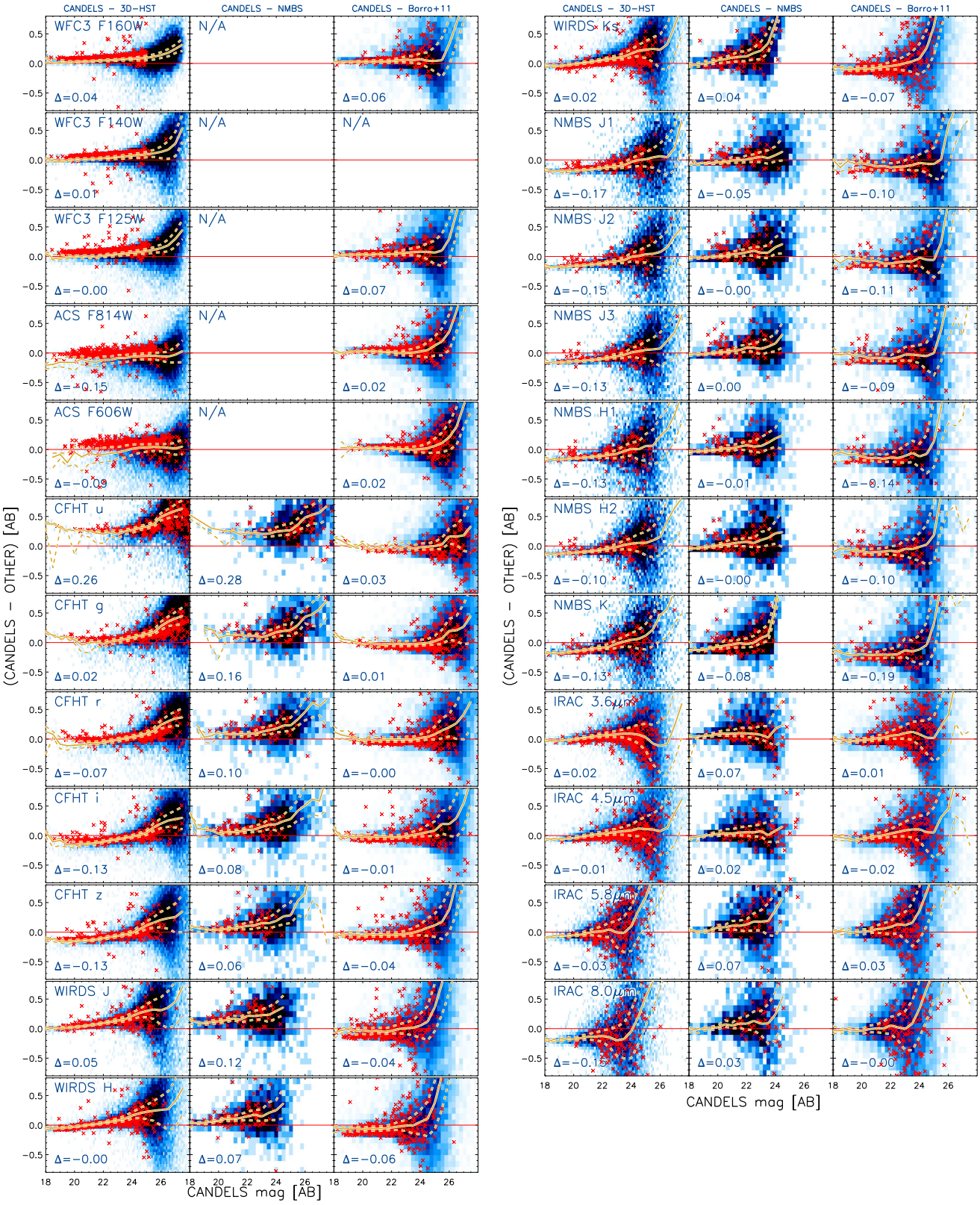

Figure 14. Comparison of CANDELS EGS 22-band photometry (as labeled in the left-side panels) to three publicly available multi-wavelength catalogs for EGS: 3D-*HST*, NMBS, and Barro+2011 (Barro et al. 2011a; left to right columns, respectively). The blue density map represents each full matching data set, while the red crosses mark objects with CLASS_STAR > 0.95 and F160W < 25 mag. The solid yellow curve marks the running median, while the dashed curves encompass the 68% of points. The number reported in the lower-left corner of each plot represents the median of the offset for the bright-end of the distribution (arbitrarily chosen to be $m < 22$ mag, $m < 21$ mag and $m < 22$ mag for 3D-*HST*, NMBS and Barro+2011, respectively).

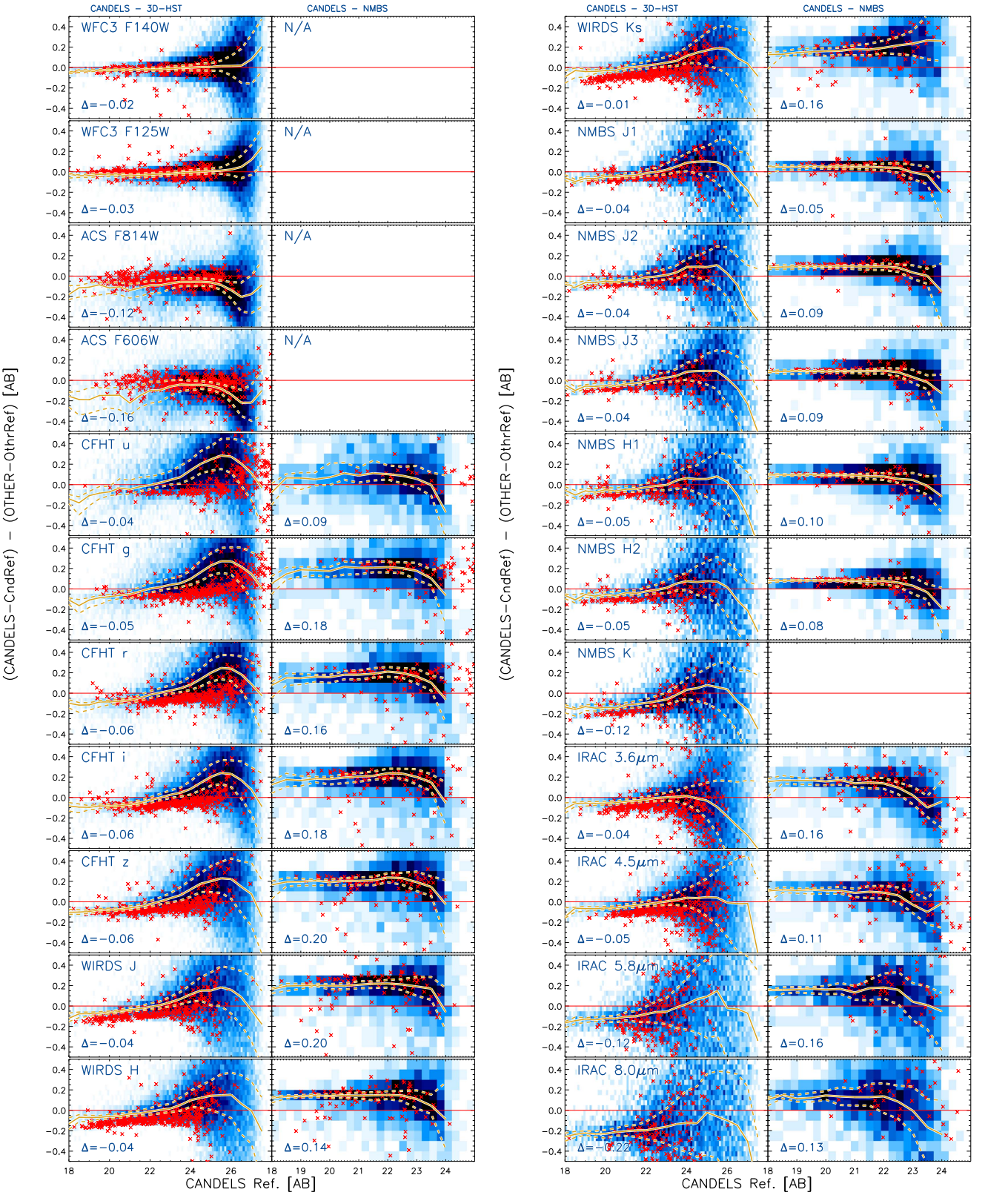

Figure 15. Comparison of CANDELS EGS colors to the publicly available multi-wavelength catalogs from 3D-*HST* and NMBS. Zeropoint offsets and Galactic extinction corrections have been removed from the 3D-*HST* and NMBS photometry. The plots present the quantity $(m_x - m_{\rm ref})_{\rm CANDELS} - (m_x - m_{\rm ref})_{\rm Other}$ as a function of $m_{\rm x,CANDELS}$, where $m_{\rm x}$ is the magnitude in band x, $m_{\rm ref}$ is the magnitude in the band that has been used by each team to recover total fluxes, and the suffix Other refers to either 3D-*HST* or NMBS. Specifically, for 3D-*HST*, $m_{\rm ref}$ corresponds to the magnitude in the WFC3/F160W band, while for NMBS it corresponds to the NEWFIRM K band. Other plotting conventions are the same as in Figure 14.

Figure 14 shows the flux comparison between the CANDELS/EGS and 3D-*HST* catalogs. In general, the agreement is good to excellent. The offsets vary from ∼0.02 mag (e.g., *HST*/WFC3, WIRCAM/WIRDS) to ∼0.2 mag (e.g., CFHT u^*, NMBS $J1$, and IRAC 5.8 μm). However, in most cases, the difference between the two catalogs is not a simple offset but has a dependence on the flux, i.e., the difference increases at fainter magnitudes.

The differences and their flux-dependent behavior likely stem from the various systematic corrections that the 3D-*HST* catalog has applied, namely, the total flux recovery on an object-by-object basis, the photometric zeropoint adjustments and the Galactic foreground extinction corrections.

A comparison of colors is more straightforward in this context, as this largely (though still not completely) circumvents the differences in the total flux recovery. This comparison is shown in Figure 15, where we use the colors relative to F160W, i.e., we consider $(m_x - m_{\rm F160W})_{\rm CANDELS} - (m_x - m_{\rm F160W})_{\rm 3D\text{-}HST}$, where m_x is the magnitude in band x. The colors based on the 3D-*HST* catalog were computed after the removal of the zeropoint adjustments and the Galactic foreground extinction corrections. Indeed, our limited knowledge on the galaxy SEDs, especially at cosmological distances, prevents us from a determination of zeropoint adjustments to levels better than ∼20% (see, e.g., the comparison of galaxy SEDs with observed photometry of Brown et al. 2014, but also, e.g., Brammer et al. 2008, for an attempt to deal with this problem using a template error function). Furthermore, as we already pointed out in Section 4.4, the amount of extinction correction depends on the specific model adopted. For these reasons, we believe that a more direct comparison between different catalogs would be more meaningful when made without either of these corrections.

The agreements in all bands are now much improved as compared to Figure 14, which supports our interpretation mentioned above. Specifically, the ∼0.2 mag offsets observed for some of the CFHT and NMBS bands have been largely reduced.

Considering that the flux comparisons done using the colors relative to the F160W band have the main effect of removing any dependence on aperture correction, the reduced offset and the flattening of the color difference as a function of magnitude suggest that the offsets and trend observed in Figure 14 for these bands are likely the result of the corrections applied to the 3D-*HST* photometry to convert aperture fluxes into total fluxes. The agreement at the faint end is not as good as in the bright regime, which can be attributed to the smaller S/N for fainter sources and larger background flux. Nevertheless, all of this suggests that the flux measurements in both catalogs have been performed in a self-consistent manner.

5.4.2. NMBS

The NMBS survey (Whitaker et al. 2011) was a medium-band NIR survey over the AEGIS and COSMOS fields. Source detection was performed on the K band. Flux measurements for the optical and NIR images were performed by using `SExtractor` in dual-image mode on the mosaics PSF-matched to the broadest PSF (i.e., the PSF of the $H1$ band). The K-band Kron (1980) fluxes were converted to total fluxes using a prescription similar to that adopted for the 3D-*HST* F160W total fluxes (see Whitaker et al. 2011 for details). The aperture fluxes for the *Spitzer* IRAC bands were measured using a procedure very similar to that used for the 3D-*HST* photometry and converted to total flux using the ratio between the total and aperture flux in the K band. The NIR medium-band filters pinpoint the Balmer/4000 Å break at $1.5 \lesssim z \lesssim 3$, allowing for accurate photometric redshift measurements of objects in this range of redshifts. Because NMBS was carried out before the CANDELS project started, the multi-wavelength photometric catalog does not include *HST*/WFC3 data.

Figure 14 shows that the fluxes from both catalogs agree reasonably well with each other, with the absolute differences generally being within ∼0.1 mag in the bright regime. Similar to the case for 3D-*HST*, the differences show a flux-dependent trend, which is likely due to the systematic corrections applied in the NMBS catalog. Comparison of the difference in colors (Figure 15) shows much improved agreement in the sense that the flux-dependent behavior is largely removed. The amplitudes of the systematic offsets are similar to those found by the 3D-*HST* team (see, e.g., Figure 34 of Skelton et al. 2014).

Table 3
List of Average Zeropoint Offsets Applied to the Photometric Catalog

Band	$ZP_{\rm factor}$[a]
CFHT u^*	1.05249
CFHT g'	0.988473
CFHT r'	0.998439
CFHT i'	0.991876
CFHT z'	0.993045
ACS F606W	0.936776
ACS F814W	0.972712
WFC3 F125W	1.02849
WFC3 F140W	1.02231
WFC3 F160W	1.03405
WIRCam K_S	0.964757
NEWFIRM K	0.883957
IRAC 3.6 μm	1.00648
IRAC 4.5 μm	0.993963
IRAC 5.8 μm	1.0
IRAC 8.0 μm	1.0

Note.
[a] The zeropoint offsets are such that $\rm Flux_{corrected} = ZP_{factor} \times Flux_{original}$. The zeropoint offsets were applied only for photometric redshift estimates. No zeropoint correction is present in the multi-wavelength photometric catalog.

5.4.3. Barro+2011

The multi-wavelength photometric catalog of Barro et al. (2011a) was assembled by cross-matching the `SExtractor` detections in IRAC 3.6 and 4.5 μm to the detections performed independently in each band, using a search radius of 2.″0 Subaru R-band imaging was used to reduce the multiple matches arising from the larger IRAC PSF. Photometry was carried out in each band using the Kron (1980) elliptical aperture obtained from the Subaru R-band mosaic. When multiple counterparts to IRAC sources were found, IRAC fluxes were measured in 0.″9 apertures after deblending using a template-fitting algorithm similar to that implemented in `TFIT`. Total magnitudes in the IRAC bands for such sources were finally calculated by applying the aperture corrections derived from the PSF growth curves.

The comparison between the CANDELS EGS photometry and that of Barro et al. (2011a; Figure 14) shows a very good

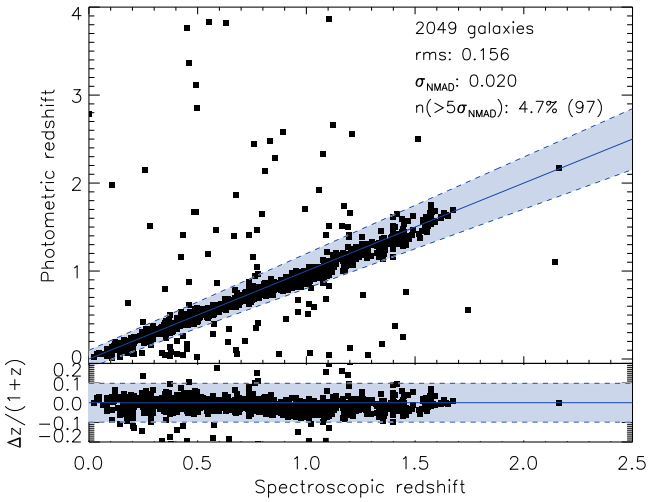

Figure 16. Comparison between the spectroscopic redshifts from DEEP2+3 and the CANDELS photometric redshifts. Sources with detection in the X-ray and CLASS_STAR > 0.85 were excluded from the sample. The top panel shows the direct comparison between the spectroscopic redshifts and photometric redshifts, while the bottom panel presents $(z_{phot} - z_{spec})/(1 + z_{spec})$. In both panels, the solid blue line indicates the 1:1 correspondence, while the filled light-blue region encompasses the region within $5 \times \sigma_{NMAD}$.

agreement for most of the bands, with offsets of $\lesssim$0.1 mag for the brighter sources. We do not show any color comparisons in Figure 15 corresponding to what we do in Sections 5.4.1 and 5.4.2; indeed, such a comparison would not have the advantages as in the previous two cases because no further corrections were applied to the SExtractor flux_auto measurements for all bands.

5.4.4. Summary

In this section, we compared the flux measurements in all bands from our catalog to the corresponding ones of the matching objects of three public catalogs: Skelton et al. (2014), Whitaker et al. (2011), and Barro et al. (2011a). Since each team assembled their catalog using different tools and/or configurations and implemented different ways of measuring total fluxes, we considered two different approaches: (1) we compared the total fluxes as directly provided by each team, and (2) we compared fluxes as closely as possible to those initially recovered from the mosaics, removing any further correction that was successively applied (e.g., zeropoint adjustments, galactic extinction, aperture corrections). As such, comparisons in this second case should provide a more reliable check on whether systematics in flux measurements exist between two different catalogs. We presented the comparisons in Figures 14 and 15, respectively.

Figure 14 shows that overall the flux measurements in our catalog systematically differ from those in the other three catalogs by up to ~10%, with only a few cases of systematic differences reaching ~20%. However, trends with magnitude are also present. These trends are almost totally absent when comparing to Barro et al. (2011a), while they are more visible when comparing to Skelton et al. (2014) and Whitaker et al. (2011). This flux-dependent behavior likely arise from the systematic corrections that were applied, namely, the total flux recovery on an object-by-object basis, the photometric zeropoint adjustments and the Galactic extinction corrections.

In order to provide a first test to the above hypothesis, in Figure 15, we presented a comparison after removing zeropoint corrections, galactic extinction, and considering a comparison in colors relative to the F160W flux. Indeed, the trends with magnitude decreased sensibly or even disappeared. The average offsets are within 0.1 mag for the Skelton et al. (2014) case, which increases the confidence on our flux measurements, though, for Whitaker et al. (2011), we register an increase in offset values. As the main effect of considering differences between colors relative to the detection band is to cancel any systematics from aperture correction, the reduced trends strongly suggest that the disagreement observed for some of the bands in Figure 14 are the result of the aperture corrections applied by the other teams.

The origins of systematic errors of the order of up to 10% are very difficult to track because they could be a consequence of different mixtures of fine-tuning parameters for mosaic creation (including zeropoint determinations), background subtraction, analysis thresholds, and other corrections to "total" fluxes. Although in this section we presented the comparison to public catalogs, the assessment of the origin of such systematics goes beyond the scope of this paper.

6. Photometric Redshifts and Stellar Masses

Using the multi-wavelength photometry presented in the previous sections, we derived photometric redshifts and stellar masses for all the sources in the catalog, measured following the methods of Dahlen et al. (2013) and Mobasher et al. (2015), respectively. We remind the reader that our catalog also contains a match to 246 X-ray sources, which are likely AGNs. Appropriate measurement of their photometric redshifts and stellar masses requires the inclusion of SED templates, which take into account the AGN contribution, resulting in otherwise unreliable values. For this reason, for these sources, we include the photometric redshift values from Nandra et al. (2015) computed adopting specific priors and SED templates (see also Appendix C).[38] Also, stellar masses for such objects should be computed taking into account the presence of the AGN affecting optical and NIR data, which could otherwise boost the stellar mass measurement. At this stage, this part of the computation is not ready and for these sources masses should be considered upper limits.

6.1. Photometric Redshifts

The multi-band photometric data were independently analyzed by 10 different groups within the CANDELS collaboration. Each group adopted a different code and/or set of SED templates.[39] The NMBS *J*1, *J*2, *J*3, *H*1, and *H*2 data were excluded because of their relatively shallow depth and the limited overlap with the F160W footprint. The WIRCAM J and H data were also excluded because these two bands are similar to the WFC3 F125W and F160W, respectively, but the data are much shallower than the latter two. As a training set, 840 spectroscopic redshifts from the DEEP3 program were

[38] These photometric redshifts and the associated *P(z)* are also available from http://www.mpe.mpg.de/XraySurveys/AEGIS-X.

[39] Overall, our adopted SED templates (Dahlen et al. 2013; Mobasher et al. 2015) did not include heated dust emission, which will only impact the IRAC 5.8 and 8.0 μm bands when the objects are at very low redshifts ($z \lesssim 0.3$). However, only a very small number of objects in our catalog could be impacted. Only 187 objects (~0.4% of the full catalog) are expected to be at $z \lesssim 0.3$ and might be impacted by dust emission (having S/N > 3 in 5.8 μm).

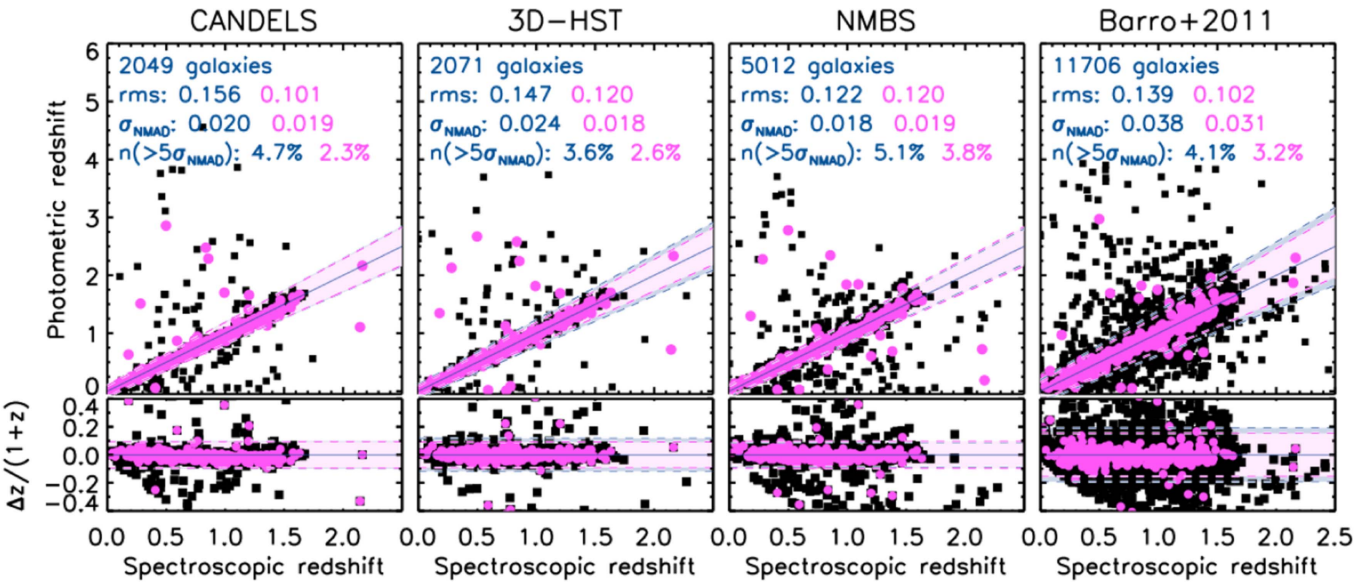

Figure 17. Comparison between the spectroscopic redshifts from DEEP2+3 and the photometric redshifts from this work, the 3D-*HST* survey, NMBS, and Barro et al. (2011b), left to right, respectively. The magenta points mark the sources in common among the three catalogs with DEEP2+3 spectroscopic redshift, not detected in the X-ray and with CLASS_STAR < 0.85 (558 objects). The labels present the dispersion and fraction of outliers for the full sample and for the subsample in common among the three surveys (blue and magenta labels, respectively). The $5\sigma_{\rm NMAD}$ limits for the full and for the common samples are indicated by the light-blue and pink regions respectively.

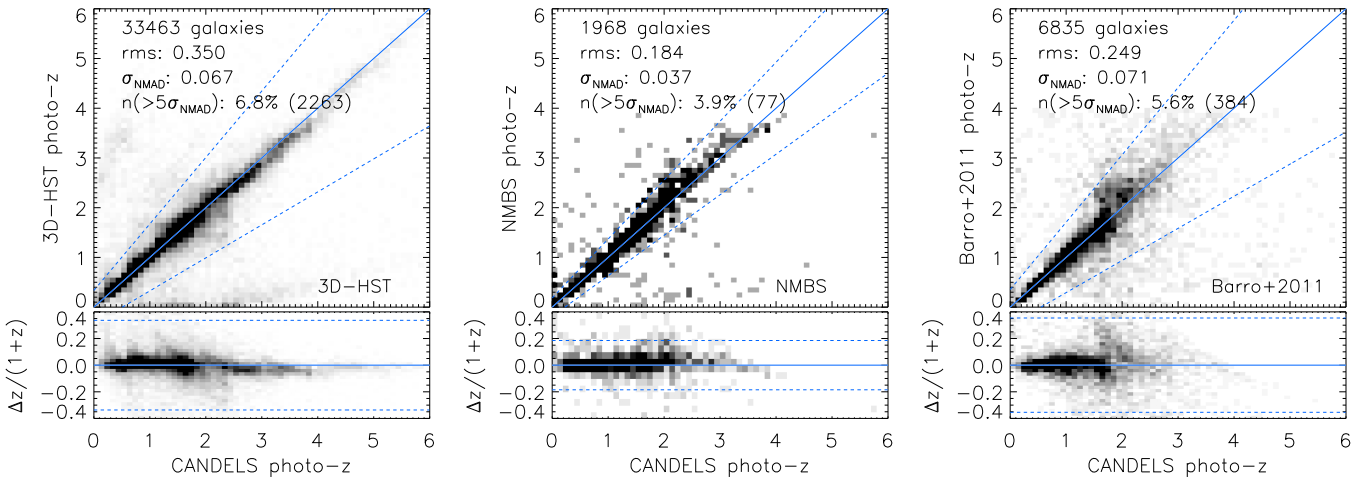

Figure 18. Top panels: comparison between the photometric redshifts measured using the CANDELS multi-wavelength photometric catalog and the photometric redshifts of the matching sources from three public catalogs: 3D-*HST* (Skelton et al. 2014), NMBS (Whitaker et al. 2011), and Barro et al. (2011b), left to right panel, respectively. The comparison is shown in the form of a density plot, with darker regions corresponding to an underlying higher density of population. The solid blue line marks the 1:1 relation, while the dashed lines delimit the $5 \times \sigma_{\rm NMAD}$ region. Indicated by the labels are the $\sigma_{\rm NMAD}$ and the fraction of objects lying outside the $5 \times \sigma_{\rm NMAD}$ region ($n(>5\sigma_{\rm NMAD})$); the number in parenthesis indicates the total number of outliers. Bottom panels: same as above, but showing $(z_{\rm phot,X} - z_{\rm phot,CND})/(1 + z_{\rm phot,CND})$ as a function CANDELS photometric redshifts, where $z_{\rm phot,X}$ is the photometric redshift from the catalog X. Most of the galaxies show consistent photometric redshift measurements across the three catalogs, with negligible offset. The dispersion is characterized by a $\sigma_{\rm NMAD} \lesssim 0.07$ and a fraction of catastrophic outliers below 7%.

also provided to each team. As a common practice, the photometric zeropoints were fine-tuned by each group during the process in order to minimize the overall residuals between the measured flux densities and those expected from the best-fit templates. Such fine adjustments varied slightly among groups due to the differences in their methods and their adopted template libraries. For this reason, the multi-wavelength photometric catalog does not include such offsets. However, the average photometric zeropoint offsets adopted by each group are reported in Table 3.

A number of codes for the measurements of photometric redshifts are available today (see, e.g., Dahlen et al. 2013 for a list). However, discrepancies in the redshift measurements still exist among themselves and with respect to spectroscopic redshifts. Using spectroscopic redshifts as reference, Dahlen et al. (2013) showed that the median of their 13 sets of photometric redshifts provide the best measurements. This is most likely because systematic effects among these 13 groups have canceled out when taking the median. For this reason, and because most of the 10 configurations adopted in this work for

Table 4
Configurations Adopted by Each Team for the Measurement of Stellar Masses

Label[a]	Code	SSP[b]	SFH[c]	$Z/Z_{\odot}$	IMF	Neb. Lines
M2	FAST (Kriek et al. 2009)	BC03	τ	1	Chabrier (2003)	no
M6	own (PI: Fontana)	BC03	τ	1	Chabrier (2003)	no
M10	HyperZ (Bolzonella et al. 2000)	MA05	τ, const., trunc.	0.2–2.5	Chabrier (2003)	no
M11	Le Phare (Ilbert et al. 2006)	BC03	τ	0.4, 1	Chabrier (2003)	yes
M12	WikZ (Wiklind et al. 2008)	BC03	del-τ	0.2–2.5	Chabrier (2003)	no
M13	FAST (Kriek et al. 2009)	BC03	τ	1	Chabrier (2003)	no
M14	SpeedyMC (Acquaviva et al. 2012)	BC03	τ, del-τ, const., lin. incr., incr.-τ	1	Chabrier (2003)	yes
M15	own (Lee et al. 2010)	BC03	del-τ	0.2–2.5	Chabrier (2003)	no

Notes.
[a] Labels as defined in Mobasher et al. (2015).
[b] Simple stellar population models are BC03 ≡ Bruzual & Charlot (2003) and MA05 ≡ Maraston (2005).
[c] Star formation histories are $\tau \equiv$ exponentially declining; const. ≡ constant; trunc. ≡ exponentially decreasing with truncation; del-$\tau \equiv$ delayed exponential (SFH $\propto t \times \exp(-t/\tau)$); lin. incr. ≡ linearly rising; and incr.-$\tau \equiv$ exponentially rising.

the measurement of photometric redshifts coincide with those of Dahlen et al. (2013), we adopted the median of the 10 photometric redshift estimates as the final measurements in our catalog. Figure 16 presents the comparison of these photometric redshifts to the DEEP2+3 spectroscopic redshifts when available. Our photometric redshifts are tightly distributed around the spectroscopic redshifts, with a low dispersion of $\sigma = 0.020$ and only ∼5% catastrophic outliers, defined as a $>5\sigma$ difference between photometric and spectroscopic redshifts. The distribution of catastrophic outliers shows a peak at $z_{\rm phot} \sim 0.1$. We selected the outliers with $z_{\rm phot} < 0.2$. This subsample included 20 galaxies. Visual inspection of their SEDs revealed that 17 sources are characterized by strong emission lines, while the photometry of the remaining 3 objects shows inconsistent measurements in several bands.

6.2. Comparison to Other Photometric Redshift Catalogs

A number of different groups have derived photometric redshifts in the EGS field (Bundy et al. 2006; Ilbert et al. 2006; Barro et al. 2011b; Whitaker et al. 2011 and Skelton et al. 2014). Here we compare our CANDELS photometric redshifts to those from three other public catalogs, namely, the 3D-*HST* (Skelton et al. 2014), the NMBS (Whitaker et al. 2011), and Barro et al. (2011b) measurements. As mentioned in Section 5.4, these three programs have covered a wide wavelength range and also include IRAC data, which are key for more accurate redshift measurements.

The photometric redshifts for the 3D-*HST* catalog were determined with the EAzY software (Brammer et al. 2008) using linear combinations of a set of seven templates from the PÉGASE models (Fioc & Rocca-Volmerange 1997) with the addition of a young and dusty template and of a red and old template from Whitaker et al. (2011). For the NMBS catalog, photometric redshifts were measured using EAzY and adopting its default template set, generated from the PÉGASE population synthesis code (see Brammer et al. 2008 for details) with the addition of a young and dusty template and of an old, red galaxy (Whitaker et al. 2011). The photometric redshifts of Barro et al. (2011b) were derived using the rainbow code (Pérez-González et al. 2008) and the PÉGASE model templates. Figure 17 shows the accuracies of these three sets of photometric redshifts by comparing to the spectroscopic redshifts from the DEEP2+3 catalogs. The different number of objects with spectroscopic redshifts in each catalog is the result of the different detection band, depths, and overlap of the detection band with the DEEP2+3 footprint. In this comparison, the NMBS results show slightly lower dispersion around the spectroscopic redshifts with respect to the other two sets, which could be due to its five medium-band NIR filters that can better pinpoint the Balmer/4000 Å break at $z \lesssim 2.5$. The higher dispersion of Barro et al. (2011b) photometric redshift measurements compared to the other catalogs is likely the result of the absence of deep NIR data bracketing the Balmer/4000 Å break,[40] and it highlights the importance of the inclusion of deep NIR data in the measurement of photometric redshifts.

Figure 18 compares these three sets of photometric redshifts to CANDELS. The agreement shows <7% of catastrophic outliers. At $z \gtrsim 2$, the 3D-*HST* photometric redshifts appear to be systematically lower than ours by $\Delta z/(1+z) \sim 0.04$. The agreement with the NMBS ones is significantly better than the other two sets (a factor $\gtrsim$1.5×). This is partly because NMBS is the shallowest among all, and thus the objects going into this comparison are predominantly the brighter ones in our catalog, which have higher accuracies. The systematically higher photometric redshifts of Barro et al. (2011b) for $z \gtrsim 2$ are likely the result of the lower S/N NIR data available in the catalog of Barro et al. (2011a). Indeed, the Balmer break enters the *J* band at $z \sim 1.7$. Shallower data in the *J* band can favor photometric redshift solutions where the Balmer break has actually already left the *J* band and has entered the *H* band, even in those cases where the Balmer break still lies in the *J* band. The net effect is thus to bias the redshift measurement toward higher values. The observed offset values in photometric redshift measurement are consistent with this hypothesis. At $z \gtrsim 2.5$, the effect is less marked as the SED immediately blueward of the Balmer break is probed by both the *J* and *H* bands, increasing the effective S/N of the break. These plots indicate that the main sources of discrepancy in photometric/spectroscopic redshifts between different methods are the sources that are not in common. For these, other things might be wrong as well, such as spectroscopic redshifts, matching, and identification.

6.3. Stellar Masses

Stellar masses have been calculated by eight groups. For each object, the redshift was fixed to either the photometric redshift adopted by our catalog or the DEEP3 spectroscopic redshift if

[40] Although in Figure 14 we compare to the *HST* WFC3 band data from Barro et al. (2011a), these were not included by Barro et al. (2011b) in the computation of the photometric redshifts and stellar masses.

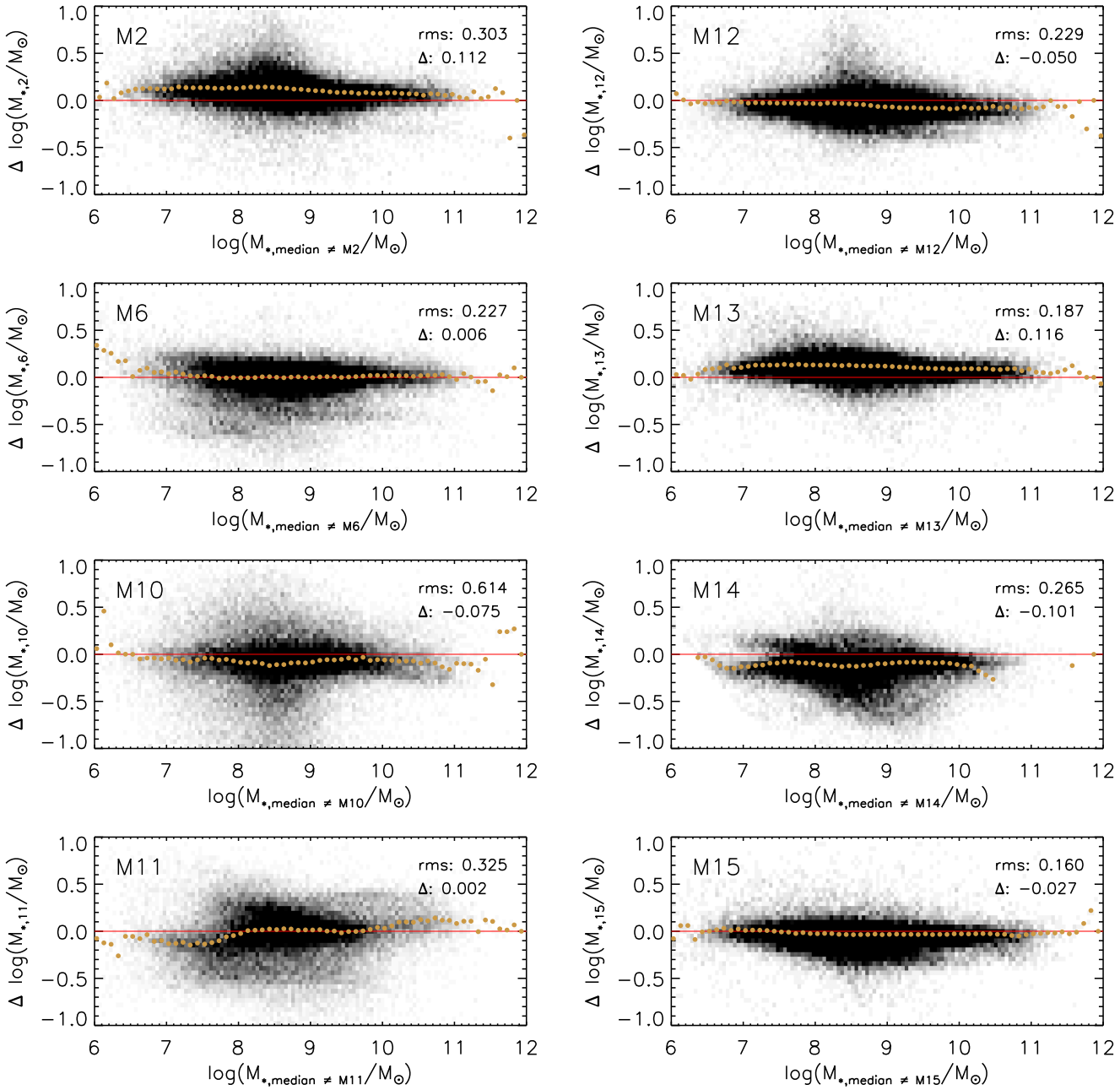

Figure 19. Comparison of the stellar mass measurements to the median of the measurements excluding that specifically considered in each plot. The vertical axis presents $\Delta \log(M_{*,n}/M_{\odot}) \equiv \log(M_{*,n}/M_{\odot}) - \log(M_{*,\mathrm{median}\neq n}/M_{\odot})$, where $\log(M_{*,n})$ is the stellar mass from group n, while $\log(M_{*,\mathrm{median}\neq n}/M_{\odot})$ is the median of the stellar mass measurements over the different groups excluding group n. Mass measurements are identified in Table 4. Yellow points are the running median. Indicated are the rms (in dex) and the median offset Δ (in dex) for the sample over the full range in stellar masses.

available. Each group adopted their choices of the fitting code, the template set, the metallicity, the SFH, the IMF, and the extinction law. The ranges and the grid step size of the free parameters also varied from one group to another. Nebular emission lines can bias the stellar mass estimates (e.g., Schaerer & de Barros 2009). For this reason, three groups computed the stellar masses separately with and without taking the nebular lines into account. Table 4 summarizes the set of configurations adopted by each group. We refer the reader to Mobasher et al. (2015) for full details. Figure 19 shows the comparisons of the stellar masses obtained by each individual group to the median of the results from other groups, excluding measurement from that one group. In this case, the two axes would be independent and the resulting comparison is free from bias. The scatter is about 20%–25% around the 1:1 relation in most cases with a median offset of ~ -0.024 dex.

The final stellar masses adopted in our catalog were computed as the median of the results from the six groups who adopted an exponentially declining SFH (with τ as free parameter) and the Chabrier (2003) IMF.

Two sets of stellar mass values are quoted in the catalog, one with the nebular line contributions taken into account and the other one without. Figure 20 compares the two measurements. Overall, the values taking into account the nebular line contaminations are $\sim$0.1 dex smaller than the ones without, with a dispersion of

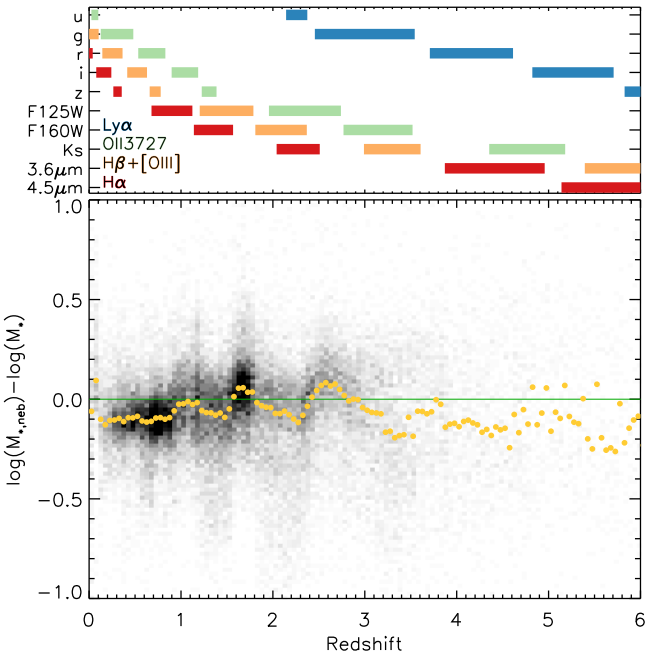

Figure 20. Top panel: cartoon of the presence of four of the stronger emission lines (Lyα, O II λ3727, Hβ+[O III], and Hα, see the legend) in a subset of bands from the CANDELS multi-wavelength photometric catalog (labeled on the vertical axis), as a function of redshift. Bottom panel: comparison between the stellar mass measurements with and without applying correction for nebular emission contamination. The yellow points mark the median of the difference of the logarithm of stellar mass across redshift, while the horizontal green line marks the 1:1 relation.

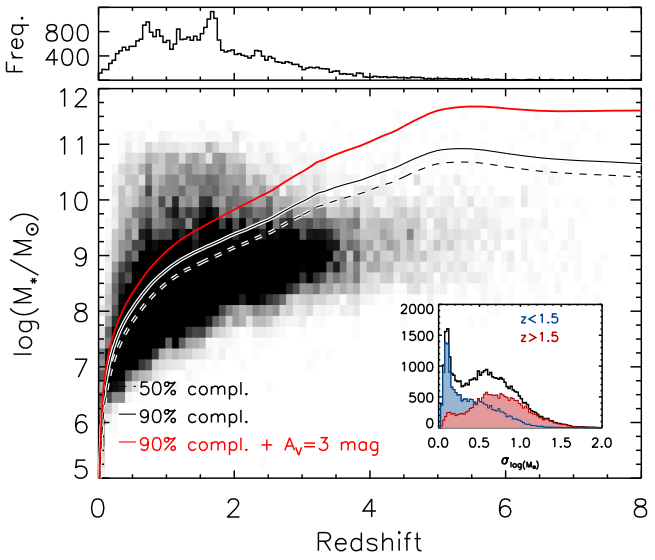

Figure 21. Top panel: photometric redshift distribution of the extended sources (SExtractor CLASS_STAR < 0.7) in the catalog in a redshift bin of 0.05. Bottom panel: distribution of the stellar mass as a function of redshifts for the full sample of extended sources (SExtractor CLASS_STAR < 0.7) in the CANDELS stellar mass catalog. Overplotted are also the 50% and 90% completeness for a (point source) passively evolving simple stellar population (SSP) from Bruzual & Charlot (2003) together with the 90% completeness of an SSP subject to a dust extinction of $A_V = 3$ mag, as indicated by the legend. The inset presents the distribution of the spread in $\log M_*$ measurements from the different adopted methods for the full sample (black line) and for objects selected to be at $z < 1.5$ and $z > 1.5$ (blue and red filled histograms, respectively, bin width 0.025 dex). The dispersions of the full sample follow a bimodal distribution. The peak with lower stellar mass measurement dispersion is mainly composed of objects at $z < 1.5$.

$\sim$0.25 dex. However, the exact trend depends on the redshift. In particular, at some specific redshift intervals, stellar mass values with the nebular line corrections are systematically larger than those obtained without this correction. One possible reason is the over-correction of the nebular line contamination in dusty and/or old stellar population SEDs (see, e.g., Figure 9 of Stefanon et al. 2015). For example, the over-correction of the [O II]λ3727 at $z \sim 2.7$ could mimic a deeper Balmer/4000 Å break, which will lead to best-fit templates being shifted to older and less luminous populations, requiring higher stellar masses.

The distribution of stellar mass with redshift is presented in Figure 21. For a passively evolving simple stellar population (SSP) model from Bruzual & Charlot (2003) with $A_V = 3$ mag, the 90% completeness in point-source detection corresponds to stellar masses $\log(M_*/M_\odot) \sim 9$, 10, 11 at $z \sim 1$, 2, 4, respectively; for $A_V = 0$ the stellar mass limits become $\log(M_*/M_\odot) \sim 8.7$, 9.2, 10.5 at $z \sim 1$, 2, 4. Most galaxies lie below the completeness limit from the passively evolving SSP model. Indeed, the majority of galaxies are star forming, implying mass-to-light ratios lower than for the quiescent galaxies. In the inset of Figure 21, we show the distribution of the spread in measurement in stellar mass resulting from the different methods. The distribution is characterized by a bimodality, around $\sigma_{\log(M_*)} \sim 0.3$ dex, with the peak corresponding to the lower dispersion regime mostly populated by objects at $z < 1.5$.

6.4. Comparison to Other Stellar Mass Catalogs

The configurations adopted by each program for the computation of stellar masses are summarized in Table 5. In addition, the three programs adopted solar metallicity, Calzetti et al. (2000) dust extinction law and did not apply any correction for nebular emission contamination. Figure 22 shows the comparisons of their stellar mass measurements to CANDELS, which suggest reasonable agreements among these different derivations. The offsets measured over the stellar mass range of $8 < \log(M_*/M_\odot) < 11$ vary between ~ -0.40 dex and $\sim$0.40 dex, with rms values of $\lesssim$0.5 dex. In comparison to the 3D-*HST* results, the agreement at $\log(M^*/M_\odot) < 9$ is excellent. At $\log(M^*/M_\odot) > 9$, the 3D-*HST* stellar masses are systematically higher by $\gtrsim$0.1 dex. Comparing to the NMBS values, similar to the case of the photometric redshift comparison (Section 6.1), the agreement is excellent (with an rms of $\sim$0.3 and $\lesssim$0.1 dex offset). The comparison to the stellar masses from Barro et al. (2011b) is made after applying an offset of -0.25 dex to their values to convert from the Salpeter IMF to the Chabrier IMF. The agreement is reasonable; at stellar masses of $\log(M^*/M_\odot) \lesssim 9$ there is an indication of an increasing trend with stellar masses, though this can be the result of the lower S/N data adopted by Barro et al. (2011b).

Since each collaboration adopted different measurements of photometric redshifts for the same object, the systematic differences in stellar mass registered in Figure 22 could be, at least in part, the result of the different input redshifts. Figure 23 therefore compares the offsets in photometric redshift to the offsets in stellar mass between the CANDELS measurements and the corresponding measurements from 3D-*HST*, NMBS, and Barro et al. (2011b). The plots show that for 3D-*HST* and NMBS there is a correlation between the offset in photometric redshifts and the offset in stellar mass. This could indeed explain the lower values in

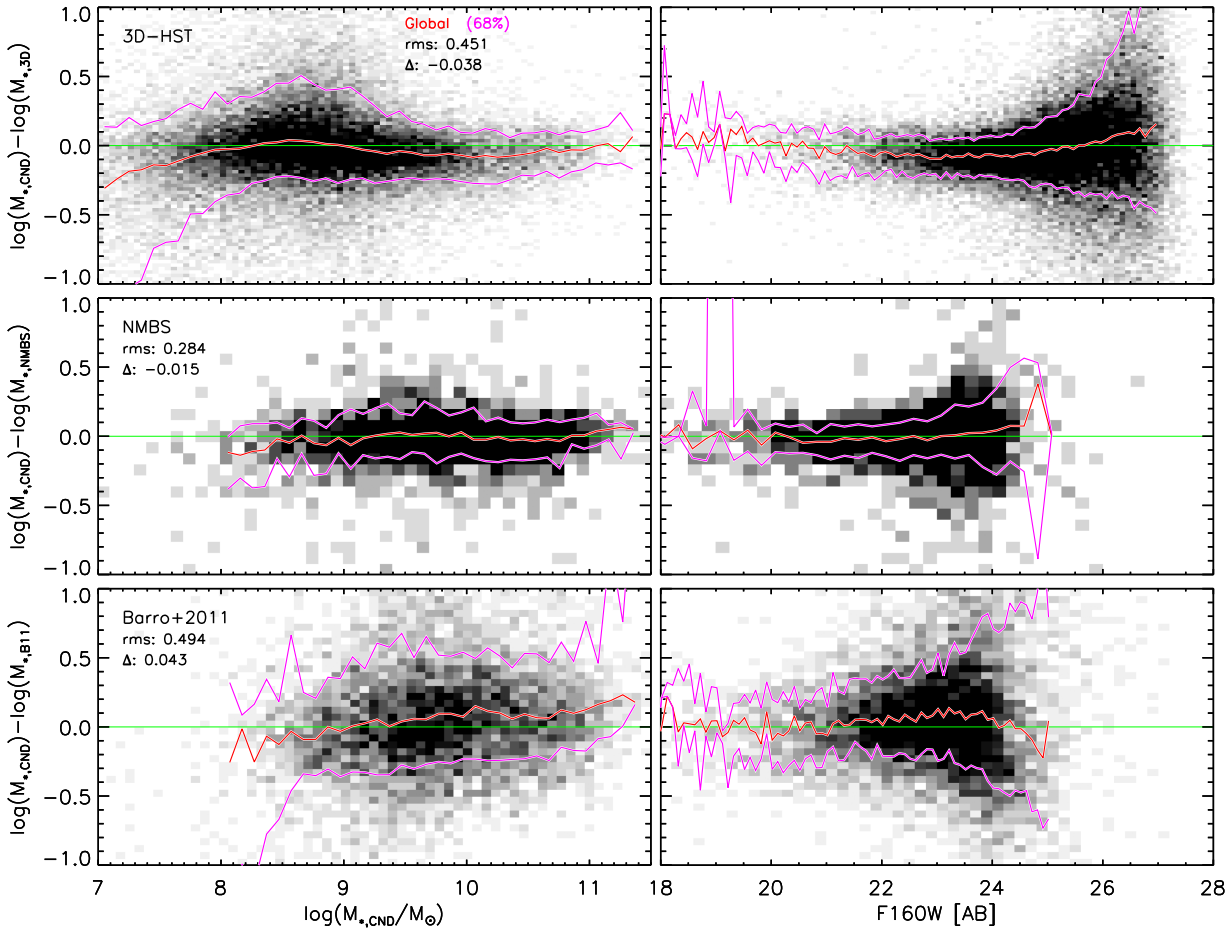

Figure 22. Left-side column: comparison of the stellar mass measurements from the CANDELS photometric catalog to the stellar mass measurements of the matching objects in three public catalogs: 3D-*HST* (Skelton et al. 2014), NMBS (Whitaker et al. 2011), and Barro et al. (2011b), top to bottom, respectively. The identity is marked by the horizontal green line. The solid red line marks the median of the difference between the logarithm of the stellar mass, while the two magenta curves encompass 68% of the points. Indicated are also the rms (in dex) and the median offset Δ (in dex). Right-side column: difference in stellar mass as a function of the CANDELS F160W magnitude. Same plotting conventions as above.

Table 5
Configuration Adopted by Three External Programs for the Computation of Stellar Masses[a]

Catalog	Code	SSP	SFH	IMF
3D-*HST*	FAST (Kriek et al. 2009)	BC03	del-τ	Chabrier (2003)
NMBS	FAST (Kriek et al. 2009)	BC03	τ	Chabrier (2003)
Barro et al. (2011b)	Rainbow (Pérez-González et al. 2008)	PÉGASE	τ	Salpeter (1955)

Note.
[a] Same abbreviations as for Table 4.

stellar mass in our catalogs compared to those in 3D-*HST* and NMBS, as for a given observed SED, a lower redshift (as measured by CANDELS) must correspond to a lower luminosity and hence stellar mass.

7. Conclusions

The core of the multi-wavelength photometric catalog produced by the CANDELS team for the AEGIS/EGS field was built on the CANDELS *HST* data in the WFC3 F125W and F160W and the ACS F606W and F814W bands. Altogether, these data provide photometry in 22 bands that cover a wavelength range of 0.4–8.0 μm. Source detection was done in the WFC3 F160W band with an improved version of `SExtractor`, which optimizes the exclusion of contaminants.

We have discovered 0.″2 position-dependent offsets between the earlier CANDELS system (based on AEGIS ACS) and that of the CFHTLS. The offsets are reduced to 0.″04 after recalibrating the astrometry to the CFHTLS system at catalog level, though we have opted to maintain the WCS of the CANDELS *HST* mosaics

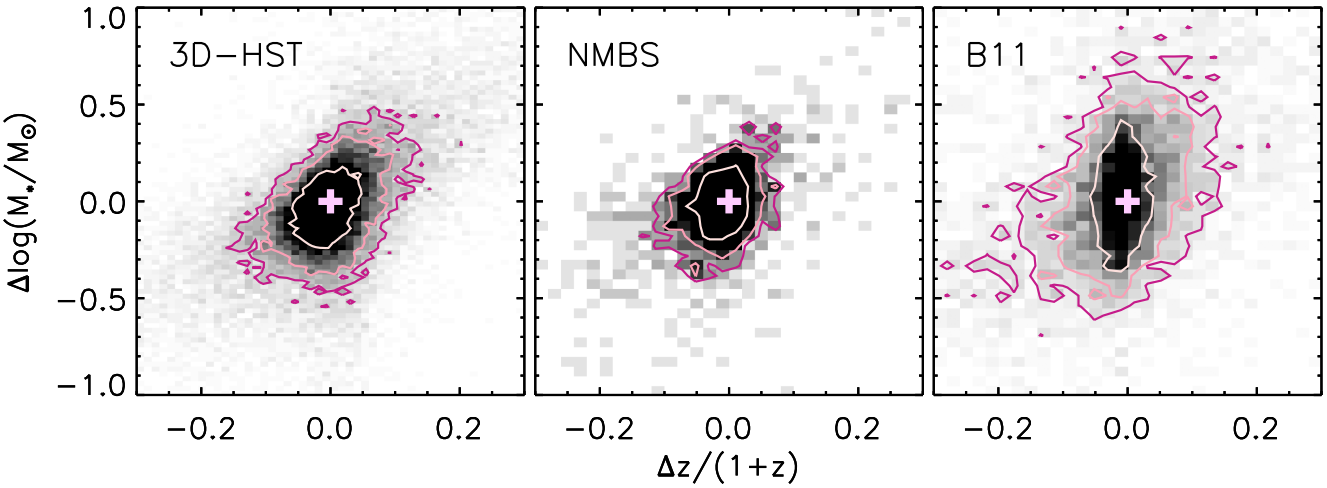

Figure 23. The panels show $\Delta\log(M_*/M_\odot) \equiv \log(M_*/M_\odot)_{\rm CANDELS} - \log(M_*/M_\odot)_{\rm Other}$ vs. $\Delta z/(1+z) \equiv (z_{\rm CANDELS} - z_{\rm Other})/(1+z_{\rm CANDELS})$, where Other refers to the survey indicated by the label on the top of each panel, and z is the photometric redshift. Overplotted are the contours corresponding to 0.05, 0.1, and 0.3 times the peak value of the distribution. For reference, a cross marks the [0, 0] position.

in this version. We release *HST* mosaic versions with both tangential planes of the AEGIS and CFHTLS astrometric systems.

The comparison of our photometry to that from the 3D-*HST*, NMBS, and Barro et al. (2011a) public catalogs shows good to excellent agreement after the various systematic corrections have been taken into account (median offsets are −0.04 mag and 0.14 mag comparing to 3D-*HST* and NMBS, respectively). Nevertheless, there are still flux-dependent offsets between our measurements of the fluxes and those of the 3D-*HST* after the zeropoint adjustments and the Galactic extinction corrections have been removed from the latter. Such flux-dependent offsets are also present when compared to the NMBS results, though to a lesser degree. We argue that these differences are due to the flux-dependent aperture corrections in the other catalogs.

We also present the catalog of photometric redshifts and stellar mass measurements. Photometric redshifts were independently measured by 10 groups within the CANDELS team, each one adopting their choices of the fitting code, the algorithm and the template library. The individual measurements were then combined together using a bayesian approach on the *P(z)* described by Dahlen et al. (2013). The comparison to the spectroscopic redshifts from the DEEP2+3 survey show a dispersion of $\sigma_{\rm NMAD} \sim 0.013$ and fraction of catastrophic outliers $n_{>5\sigma_{\rm NMAD}} \sim 7\%$.

Stellar masses were also computed independently by eight teams. The final measurement of the stellar mass is then taken to be the median of the measurements, done on a per-object basis. We estimated a conservative stellar mass limit with a maximally red SED template (i.e., a passively evolving population with $A_V = 3$ mag). The depth of the catalog corresponds to a stellar mass completeness of 90% for $\log(M_*/M_\odot) \sim 9$ at $z \sim 1$, $\log(M_*/M_\odot) \sim 10$ at $z \sim 2$, and $\log(M_*/M_\odot) \sim 11$ at $z \sim 4$.

Comparison of the photometric redshifts and stellar masses to the measurements provided by publicly available catalogs show that the agreement is good and does not have any strong bias.

The covered area and the photometric depth reached in the CANDELS EGS field will be of invaluable aid in the measurements of the luminosity and stellar mass functions at $1 \lesssim z \lesssim 5$. Furthermore, the full coverage and deep X-ray data make the EGS field unique for the study of the evolution of the AGN. Our catalogs are accessible on the primary CANDELS pages at MAST,[41] through the Vizier service,[42] and from the CANDELS team project website.[43]

We thank the referee for his helpful comments, which improved the paper's readability. This work is based on observations taken by the CANDELS Multi-Cycle Treasury Program with the NASA/ESA *HST*, which is operated by the Association of Universities for Research in Astronomy, Inc., under NASA contract NAS5-26555. This study makes use of data from AEGIS, a multi-wavelength sky survey conducted with the *Chandra*, *GALEX*, Hubble, Keck, CFHT, MMT, Subaru, Palomar, *Spitzer*, VLA, and other telescopes and supported in part by the NSF, NASA, and the STFC. This work is based in part on data obtained with the *Spitzer Space Telescope*, which is operated by the Jet Propulsion Laboratory, California Institute of Technology under a contract with NASA. This work is based on observations taken by the 3D-*HST* Treasury Program (GO 12177 and 12328) with the NASA/ESA *HST*, which is operated by the Association of Universities for Research in Astronomy, Inc., under NASA contract NAS5-26555. Funding for the DEEP2 Galaxy Redshift Survey has been provided by NSF grants AST-95-09298, AST-0071048, AST-0507428, and AST-0507483 as well as NASA LTSA grant NNG04GC89G. Funding for the DEEP3 Galaxy Redshift Survey has been provided by NSF grants AST-0808133, AST-0807630, and AST-0806732. Based on observations obtained with MegaPrime/MegaCam, a joint project of CFHT and CEA/IRFU, at the Canada–France–Hawaii Telescope (CFHT), which is operated by the National Research Council (NRC) of Canada, the Institut National des Science de l'Univers of the Centre National de la Recherche Scientifique (CNRS) of France, and the University of Hawaii. This work is based in part on data products produced at Terapix available at the Canadian Astronomy Data Centre as part of the

[41] https://archive.stsci.edu/prepds/candels
[42] http://vizier.u-strasbg.fr/viz-bin/VizieR
[43] http://candels.ucolick.org

Table 6
Multi-wavelength Photometric Catalog Entries

Columns #	Name	Description
1	ID	Sequential ID number in the F160W-based SExtractor catalog.
2	IAU_designation	Official IAU designation of the object.
3	RA	R.A. and decl. (J2000) in the F160W mosaic expressed is decimal degrees,
4	DEC	after they have been converted to the CFHTLS astrometric system. The values in these two columns are suggested as the coordinates of the objects in the catalog.
5	RA_Lotz2008	Original R.A. and decl. (J2000) in the F160W mosaic in decimal degrees,
6	DEC_Lotz2008	whose astrometry was calibrated using the Lotz et al. (2008) system.
7	FLAGS	Flag. A value of 1 corresponds to sources falling in regions of low S/N as it can be at the borders of the mosaic; a value of 2 indicates that a source, as identified by its footprint in the segmentation map, falls close to a bright star or to its diffraction spikes; a value of 3 indicates that the source suffers from both a low S/N and contamination from bright stars. Sources free from any of the above effects have a flag of 0.
8	CLASS_STAR	SExtractor parameter CLASS_STARfrom the F160W mosaic.
9	CFHT_u_FLUX	Columns 9–54: Flux densities and associated uncertainties, expressed in μJy. A value of -99 has
10	CFHT_u_FLUXERR	been set to the flux and associated uncertainty for those objects falling outside the coverage
11	CFHT_g_FLUX	of the mosaic in a specific band or when bad pixels within the segmentation map
12	CFHT_g_FLUXERR	contaminate the flux measurement.
13	CFHT_r_FLUX	…
14	CFHT_r_FLUXERR	…
15	CFHT_i_FLUX	…
16	CFHT_i_FLUXERR	…
17	CFHT_z_FLUX	…
18	CFHT_z_FLUXERR	…
19	ACS_F606W_FLUX	…
20	ACS_F606W_FLUXERR	…
21	ACS_F814W_FLUX	…
22	ACS_F814W_FLUXERR	…
23	WFC3_F125W_FLUX	…
24	WFC3_F125W_FLUXERR	…
25	WFC3_F140W_FLUX	…
26	WFC3_F140W_FLUXERR	…
27	WFC3_F160W_FLUX	…
28	WFC3_F160W_FLUXERR	…
29	WIRCAM_J_FLUX	…
30	WIRCAM_J_FLUXERR	…
31	WIRCAM_H_FLUX	…
32	WIRCAM_H_FLUXERR	…
33	WIRCAM_K_FLUX	…
34	WIRCAM_K_FLUXERR	…
35	NEWFIRM_J1_FLUX	…
36	NEWFIRM_J1_FLUXERR	…
37	NEWFIRM_J2_FLUX	…
38	NEWFIRM_J2_FLUXERR	…
39	NEWFIRM_J3_FLUX	…
40	NEWFIRM_J3_FLUXERR	…
41	NEWFIRM_H1_FLUX	…
42	NEWFIRM_H1_FLUXERR	…
43	NEWFIRM_H2_FLUX	…
44	NEWFIRM_H2_FLUXERR	…
45	NEWFIRM_K_FLUX	…
46	NEWFIRM_K_FLUXERR	…
47	IRAC_CH1_FLUX	…
48	IRAC_CH1_FLUXERR	…
49	IRAC_CH2_FLUX	…
50	IRAC_CH2_FLUXERR	…
51	IRAC_CH3_FLUX	…
52	IRAC_CH3_FLUXERR	…
53	IRAC_CH4_FLUX	…
54	IRAC_CH4_FLUXERR	…
55	ACS_F606W_v08_FLUX	Columns 55–62: flux densities and associated uncertainties for the AEGIS data set.
56	ACS_F606W_v08_FLUXERR	…
57	ACS_F814W_v08_FLUX	…
58	ACS_F814W_v08_FLUXERR	…

Table 6
(Continued)

Columns #	Name	Description
59	WFC3_F125W_v08_FLUX	…
60	WFC3_F125W_v08_FLUXERR	…
61	WFC3_F160W_v08_FLUX	…
62	WFC3_F160W_v08_FLUXERR	…
63	IRAC_CH3_v08_FLUX	Columns 63–66: flux densities and associated uncertainties for the IRAC 5.8 and 8.0 μm band with the old convolution kernel, which were used for the computation of photometric redshifts and stellar masses.
64	IRAC_CH3_v08_FLUXERR	
65	IRAC_CH4_v08_FLUX	
66	IRAC_CH4_v08_FLUXERR	…
67	ACS_F606W_FLUX_PHZ	Columns 67–76: flux densities and associated uncertainties for the fluxes adopted to compute photometric redshifts and stellar population parameters.[a]
68	ACS_F606W_FLUXERR_PHZ	
69	ACS_F814W_FLUX_PHZ	…
70	ACS_F814W_FLUXERR_PHZ	…
71	WFC3_F125W_FLUX_PHZ	…
72	WFC3_F125W_FLUXERR_PHZ	…
73	WFC3_F140W_FLUX_PHZ	…
74	WFC3_F140W_FLUXERR_PHZ	…
75	WFC3_F160W_FLUX_PHZ	…
76	WFC3_F160W_FLUXERR_PHZ	…
77	DEEP_SPEC_Z	Spectroscopic redshift from the DEEP2 and DEEP3 catalogs. If no match is found, the value has been set to −99.

Note.
[a] The fluxes and uncertainties in some *HST* bands and for some of the sources were initially set to −99 even if there was no indication of bad measurement. Columns 19–28 contain the fixed values. Here we include the original version of these columns as such measurements were adopted to estimate photometric redshifts and stellar population parameters. These columns are identified by the suffix _PHZ (for photo-z). Tests showed that photo-z for most of the sources were not strongly affected by this problem. However, we further OR-flag the FLAGS column with the value of 4 to reflect the 160 sources for which $\Delta z/(1+z) > 0.1$ and potential less robust stellar population parameters.

(This table is available in its entirety in machine-readable form.)

Canada–France–Hawaii Telescope Legacy Survey, a collaborative project of NRC and CNRS. Based on observations obtained with WIRCam, a joint project of CFHT,Taiwan, Korea, Canada, France, at the Canada–France–Hawaii Telescope (CFHT), which is operated by the National Research Council (NRC) of Canada, the Institute National des Sciences de l'Univers of the Centre National de la Recherche Scientifique of France, and the University of Hawaii. This work is based in part on data products produced at TERAPIX, the WIRDS (WIRcam Deep Survey) consortium, and the Canadian Astronomy Data Centre. This research was supported by a grant from the Agence Nationale de la Recherche ANR-07-BLAN-0228. This study makes use of data from the NEWFIRM Medium-Band Survey, a multi-wavelength survey conducted with the NEWFIRM instrument at the KPNO, supported in part by the NSF and NASA. This work is based in part on observations made with the *Spitzer Space Telescope*, which is operated by the Jet Propulsion Laboratory, California Institute of Technology under a contract with NASA. IRAF is distributed by the National Optical Astronomy Observatories, which are operated by the Association of Universities for Research in Astronomy, Inc., under cooperative agreement with the National Science Foundation.

Facilities: Hubble Space Telescope (ACS, WFC3), *Spitzer Space Telescope* (IRAC).

Appendix A
Content of the Photometric Catalog

Table 6 lists the columns in the multi-wavelength photometric catalog. Our catalogs are accessible on the primary CANDELS pages at MAST,[44] through the Vizier service,[45] and from the CANDELS team project website.[46]

Appendix B
Content of the Photometric Redshift Catalog

Table 7 presents the list of the columns available in the photometric redshift catalog.

Appendix C
Content of the Stellar Mass Catalog

Table 8 presents the list of the columns available in the stellar mass catalog.

Appendix D
Content of the Physical Parameters Catalog

Table 9 presents the list of the columns available in the physical parameters catalog. The number in the column name matches that in Table 4 and Mobasher et al. (2015). We refer the reader to Table 4 and Mobasher et al. (2015) for details on the configuration of each method.

[44] https://archive.stsci.edu/prepds/candels
[45] http://vizier.u-strasbg.fr/viz-bin/VizieR
[46] http://candels.ucolick.org

Table 7
Photometric Redshift Catalog Entries

Columns #	Name	
1	ID	Sequential ID number.
2	Photo_z_Median	Median of the photometric redshift measurements.
3	Photo_z_Salvato	Columns 3–8: photmetric redshift measurements from the individual group.
4	Photo_z_Mobasher	…
5	Photo_z_Finkelstein	…
6	Photo_z_Barro	…
7	Photo_z_Wiklind	…
8	Photo_z_Wuyts	…
9	D95	Accuracy of the photometric redshifts based on their confidence intervals (Dahlen et al. 2013).
10	Spec_z	Spectroscopic redshift of the control sample (−99 otherwise), from the DEEP3 catalog.
11	Photo_z_lower68	Columns 11–14: 68% and 95% confidence intervals for the median of the redshift measurements. For
12	Photo_z_upper68	details on its computation, see Section 6.1 and Dahlen et al. (2013).
13	Photo_z_lower95	…
14	Photo_z_upper95	…

(This table is available in its entirety in machine-readable form.)

Table 8
Stellar Mass Catalog Entries

Columns #	Name	Description
1	ID	Sequential ID number in the F160W-based `SExtractor` catalog.
2	RAdeg	Columns 2–3: R.A. and decl. (J2000) in the F160W mosaic.
3	DECdeg	…
4	Hmag	Magnitude in the F160W band.
5	PhotFlag	Flag in the photometric catalog.
6	Class_star	`SExtractor CLASS_STAR` parameter.
7	AGNflag	=1 for those objects with a counterpart in the Nandra et al. (2015) catalog, 0 otherwise.
8	zphot	Photometric redshift measurement.
9	zspec	Spectroscopic redshift from the DEEP3 catalog.
10	zspec_q	Quality flag for the spectroscopic redshift: 1 = Good; 2 = Fair; 3 = Poor.
11	zspec_refer	Source of the spectroscopic redshift catalog. 1 = DEEP2/3.
12	zbest	Best redshift measurement: if spectroscopic redshift is available, then `zbest = zspec`, otherwise `zbest = zphot`.
13	zphot_l68	Columns 13–16: 68% and 95% confidence intervals on the photometric redshift measurements.
14	zphot_u68	…
15	zphot_l95	…
16	zphot_u95	…
17	zphotAGN	Photometric redshifts for the sources with a match in the X-Ray catalog of Nandra et al. (2015), computed adopting AGN specific SED templates and priors (see Nandra et al. 2015 for more details).
18	M_neb_med	Columns 18–19: stellar mass measurement and associated uncertainty from the median of the logarithm of
19	s_neb_med	stellar mass measurements obtained taking into account nebular emission contamination.
20	M_med	Columns 20–21: stellar mass measurement and associated uncertainty from the median of the logarithm of
21	s_med	stellar mass measurements obtained without considering nebular emission contamination.
22	M_14a_cons	Columns 22–35: stellar mass measurements from the individual methods. See Table 4 for details on the
23	M_11a_tau	configuration of each method. The number in the name matches that in Table 4.
24	M_6a_tauˆNEB	…
25	M_13a_tau	…
26	M_12a	…
27	M_6a_tau	…
28	M_2a_tau	…
29	M_15a	…
30	M_10c	…
31	M_14a_lin	…
32	M_14a_deltau	…
33	M_14a_tau	…
34	M_14a_inctau	…
35	M_14a	…
36	M_neb_med_lin	Col 36–37: stellar mass measurement and associated uncertainty from the median of the linear value
37	s_neb_med_lin	of the stellar mass measurements obtained taking into account nebular emission contamination.
38	M_med_lin	Columns 38–39: stellar mass measurement and associated uncertainty from the median of the linear value
39	s_med_lin	of the stellar mass measurements obtained without taking into account nebular emission contamination.

(This table is available in its entirety in machine-readable form.)

Table 9
Physical Parameter Catalog Entries

Columns #	Name	Description
1	ID	Sequential ID number in the F160W-based SExtractor catalog.
2	age_2a_tau	Age from method 2*a* [log(t yr^{-1})]
3	tau_2a_tau	τ from method 2*a* [Gyr]
4	Av_2a_tau	A_V from method 2*a* [mag]
5	SFR_2a_tau	SFR from method 2*a* [$M_\odot$ yr^{-1}]
6	chi2_2a_tau	Reduced χ^2 from method 2*a*
7	age_4b	Age from method 4*b* [log(t yr^{-1})]
8	EBV_4b	$E(B-V)$ from method 4*b* [mag]
9	age_6a_tau	Age from method 6a_τ [log(t yr^{-1})]
10	tau_6a_tau	τ from method 6a_τ [Gyr]
11	EBV_6a_tau	$E(B-V)$ from method 6a_τ [mag]
12	SFR_6a_tau	SFR from method 6a_τ [$M_\odot$ yr^{-1}]
13	met_6a_tau	Gas metallicity from method 6a_τ [$Z_\odot$]
14	extlw_6a_tau	Extinction law from method 6a_τ: 1 = Calzetti; 2 = SMC
15	chi2_6a_tau	Reduced χ^2 from method 6a_τ
16	L1400_6a_tau	Rest-frame luminosity at 1400 Å from method 6a_τ (L_ν(1400 Å)[erg s^{-1} Hz^{-1}]
17	L2700_6a_tau	Rest-frame luminosity at 2700 Å from method 6a_τ (L_ν(2700 Å) [erg s^{-1} Hz^{-1}]
18	UMag_6a_tau	U rest-frame magnitude from method 6a_τ [AB system]
19	BMag_6a_tau	B rest-frame magnitude from method 6a_τ [AB system]
20	VMag_6a_tau	V rest-frame magnitude from method 6a_τ [AB system]
21	RMag_6a_tau	R rest-frame magnitude from method 6a_τ [AB system]
22	IMag_6a_tau	I rest-frame magnitude from method 6a_τ [AB system]
23	JMag_6a_tau	J rest-frame magnitude from method 6a_τ [AB system]
24	KMag_6a_tau	K rest-frame magnitude from method 6a_τ [AB system]
25	age_10c	Age from method 10*c* [log(t yr^{-1})]
26	SFH_10c	SFH from method 10*c* (1 = exponentially decreasing; 2 = constant; 3 = truncated; 4 = no solution)
27	tau_10c	τ from method 10*c* ($\tau = -99$ if SFH = 2 or 4) [Gyr]
28	met_10c	Gas metallicity from method 10*c* [$Z_\odot$]
29	M_l99_11a_tau	Lower stellar mass 99% confidence interval from method 11a_τ [log($M/M_\odot$)]
30	M_u99_11a_tau	Upper stellar mass 99% confidence interval from method 11a_τ [log($M/M_\odot$)]
31	age_11a_tau	Age from method 11a_τ [[log(t yr^{-1})]
32	SFR_11a_tau	SFR from method 11a_τ [$M_\odot$ yr^{-1}]
33	M_l68_12a	Lower stellar mass 68% confidence interval from method 12*a* [log($M/M_\odot$)]
34	M_u68_12a	Upper stellar mass 68% confidence interval from method 12*a* [log($M/M_\odot$)]
35	M_l95_12a	Lower stellar mass 95% confidence interval from method 12*a* [log($M/M_\odot$)]
36	M_u95_12a	Upper stellar mass 95% confidence interval from method 12*a* [log($M/M_\odot$)]
37	age_12a	Age from method 12*a* [log(t yr^{-1})]
38	tau_12a	τ from method 12*a* [Gyr]
39	EBV_12a	$E(B-V)$ from method 12*a* [mag]
40	met_12a	Metallicity from method 12*a* [$Z_\odot$]
41	Lbol_12a	log($L_{\rm bol}/L_\odot$), corrected for dust extinction, from method 12*a* [log($L/L_\odot$)]
42	chi2_12a	Reduced χ^2 from method 12*a*
43	age_13a_tau	Age from method 13a_τ [log(t yr^{-1})]
44	tau_13a_tau	τ from method 13a_τ [Gyr]
45	Av_13a_tau	A_V from method 13a_τ [mag]
46	SFR_13a_tau	SFR from method 13a_τ [$M_\odot$ yr^{-1}]
47	chi2_13a_tau	χ^2 from method 13a_τ
48	age_14a	Age from method 14*a* [log(t yr^{-1})]
49	SFH_14a	SFH from method 14*a* (1 = constant; 2 = linearly increasing; 3 = delayed; 4 = exponentially decreasing)
50	tau_14a	τ from method 14*a* [Gyr]
51	EBV_14a	$E(B-V)$ from method 14*a* [mag]
52	SFR_14a	SFR from method 14*a* [$M_\odot$ yr^{-1}]
53	q_14a	Fit quality (1 = Best; 2 = Good; 3 = Bad/No solution) from method 14*a*
54	age_6a_tau_neb	Age from method 6$a_\tau^{\rm NEB}$ [log(t yr^{-1})]
55	tau_6a_tau_neb	τ from method 6$a_\tau^{\rm NEB}$ [Gyr]
56	EBV_6a_tau_neb	$E(B-V)$ from method 6$a_\tau^{\rm NEB}$ [mag]
57	SFR_6a_tau_neb	SFR from method 6$a_\tau^{\rm NEB}$ [$M_\odot$ yr^{-1}]
58	met_6a_tau_neb	Gas metallicity from method 6$a_\tau^{\rm NEB}$ [$Z_\odot$]
59	extlw_6a_tau_neb	Extinction law from method 6$a_\tau^{\rm NEB}$: 1 = Calzetti; 2 = SMC
60	chi2_6a_tau_neb	Reduced χ^2 from method 6$a_\tau^{\rm NEB}$
61	L1400_6a_tau_neb	Rest-frame luminosity at 1400 Å from method 6$a_\tau^{\rm NEB}$ (L_ν(1400 Å) [erg s^{-1} Hz^{-1}]
62	L2700_6a_tau_neb	Rest-frame luminosity at 2700 Å from method 6$a_\tau^{\rm NEB}$ (L_ν(2700 Å) [erg s^{-1} Hz^{-1}]
63	UMag_6a_tau_neb	U rest-frame magnitude from method 6$a_\tau^{\rm NEB}$ [AB system]
64	BMag_6a_tau_neb	B rest-frame magnitude from method 6$a_\tau^{\rm NEB}$ [AB system]
65	VMag_6a_tau_neb	V rest-frame magnitude from method 6$a_\tau^{\rm NEB}$ [AB system]
66	RMag_6a_tau_neb	R rest-frame magnitude from method 6$a_\tau^{\rm NEB}$ [AB system]
67	IMag_6a_tau_neb	I rest-frame magnitude from method 6$a_\tau^{\rm NEB}$ [AB system]
68	JMag_6a_tau_neb	J rest-frame magnitude from method 6$a_\tau^{\rm NEB}$ [AB system]
69	KMag_6a_tau_neb	K rest-frame magnitude from method 6$a_\tau^{\rm NEB}$ [AB system]

Table 9
(Continued)

Columns #	Name	Description
70	age_6a_deltau	Age from method $6a_{\rm del}$ [$\log(t\ {\rm yr}^{-1})$]
71	tau_6a_deltau	τ from method $6a_{\rm del}$ [Gyr]
72	EBV_6a_deltau	$E(B-V)$ from method $6a_{\rm del}$ [mag]
73	SFR_6a_deltau	SFR from method $6a_{\rm del}$ [$M_\odot\ {\rm yr}^{-1}$]
74	met_6a_deltau	Gas metallicity from method $6a_{\rm del}$ [$Z_\odot$]
75	extlw_6a_deltau	Extinction law from method $6a_{\rm del}$: 1 = Calzetti; 2 = SMC
76	chi2_6a_deltau	Reduced χ^2 from method $6a_{\rm del}$
77	L1400_6a_deltau	Rest-frame luminosity at 1400 Å from method $6a_{\rm del}$ (L_ν(1400 Å) [erg s^{-1} Hz^{-1}]
78	L2700_6a_deltau	Rest-frame luminosity at 2700 Å from method $6a_{\rm del}$ (L_ν(2700 Å) [erg s^{-1} Hz^{-1}]
79	UMag_6a_deltau	U rest-frame magnitude from method $6a_{\rm del}$ [AB system]
80	BMag_6a_deltau	B rest-frame magnitude from method $6a_{\rm del}$ [AB system]
81	VMag_6a_deltau	V rest-frame magnitude from method $6a_{\rm del}$ [AB system]
82	RMag_6a_deltau	R rest-frame magnitude from method $6a_{\rm del}$ [AB system]
83	IMag_6a_deltau	I rest-frame magnitude from method $6a_{\rm del}$ [AB system]
84	JMag_6a_deltau	J rest-frame magnitude from method $6a_{\rm del}$ [AB system]
85	KMag_6a_deltau	K rest-frame magnitude from method $6a_{\rm del}$ [AB system]
86	age_6a_invtau	Age from method $6a_{\rm inv}$ [$\log(t\ {\rm yr}^{-1})$]
87	tau_6a_invtau	τ from method $6a_{\rm inv}$ [Gyr]
88	EBV_6a_invtau	$E(B-V)$ from method $6a_{\rm inv}$ [mag]
89	SFR_6a_invtau	SFR from method $6a_{\rm inv}$ [$M_\odot\ {\rm yr}^{-1}$]
90	met_6a_invtau	Gas metallicity from method $6a_{\rm inv}$ [$Z_\odot$]
91	extlw_6a_invtau	Extinction law from method $6a_{\rm inv}$: 1 = Calzetti; 2 = SMC
92	chi2_6a_invtau	Reduced χ^2 from method $6a_{\rm inv}$
93	L1400_6a_invtau	Rest-frame luminosity at 1400 Å from method $6a_{\rm inv}$ (L_ν(1400 Å) [erg s^{-1} Hz^{-1}]
94	L2700_6a_invtau	Rest-frame luminosity at 2700 Å from method $6a_{\rm inv}$ (L_ν(2700 Å) [erg s^{-1} Hz^{-1}]
95	UMag_6a_invtau	U rest-frame magnitude from method $6a_{\rm inv}$ [AB system]
96	BMag_6a_invtau	B rest-frame magnitude from method $6a_{\rm inv}$ [AB system]
97	VMag_6a_invtau	V rest-frame magnitude from method $6a_{\rm inv}$ [AB system]
98	RMag_6a_invtau	R rest-frame magnitude from method $6a_{\rm inv}$ [AB system]
99	IMag_6a_invtau	I rest-frame magnitude from method $6a_{\rm inv}$ [AB system]
100	JMag_6a_invtau	J rest-frame magnitude from method $6a_{\rm inv}$ [AB system]
101	KMag_6a_invtau	K rest-frame magnitude from method $6a_{\rm inv}$ [AB system]
102	age_10c_dust	Age from method $10c^{\rm dust}$ [$\log(t\ {\rm yr}^{-1})$]
103	SFH_10c_dust	SFH from method $10c^{\rm dust}$: 1 = exponentially decreasing; 2 = constant; 3 = truncated; 4 = no solution
104	tau_10c_dust	τ from method $10c^{\rm dust}$ ($\tau = -99$ if SFH = 2 or 4) [Gyr]
105	met_10c_dust	Gas metallicity from method $10c^{\rm dust}$ [$Z_\odot$]
106	age_14a_const	Age from method $14a_{\rm const}$ [$\log(t\ {\rm yr}^{-1})$]
107	EBV_14a_const	$E(B-V)$ from method $14a_{\rm const}$ [mag]
108	SFR_14a_const	SFR from method $14a_{\rm const}$ [$M_\odot\ {\rm yr}^{-1}$]
109	q_14a_const	Fit quality (1 = Best; 2 = Good; 3 = Bad/No solution) from method $14a_{\rm const}$
110	age_14a_lin	Age from method $14a_{\rm lin}$ [$\log(t\ {\rm yr}^{-1})$]
111	EBV_14a_lin	$E(B-V)$ from method $14a_{\rm lin}$ [mag]
112	SFR_14a_lin	SFR from method $14a_{\rm lin}$ [$M_\odot\ {\rm yr}^{-1}$]
113	q_14a_lin	Fit quality (1 = Best; 2 = Good; 3 = Bad/No solution) from method $14a_{\rm lin}$
114	age_14a_deltau	Age from method $14a_{\rm del}$ [$\log(t\ {\rm yr}^{-1})$]
115	tau_14a_deltau	τ from method $14a_{\rm del}$ [Gyr]
116	EBV_14a_deltau	$E(B-V)$ from method $14a_{\rm del}$ [mag]
117	SFR_14a_deltau	SFR from method $14a_{\rm del}$ [$M_\odot\ {\rm yr}^{-1}$]
118	q_14a_deltau	Fit quality (1 = Best; 2 = Good; 3 = Bad/No solution) from method $14a_{\rm del}$
119	age_14a_tau	Age from method $14a_\tau$ [$\log(t\ {\rm yr}^{-1})$]
120	tau_14a_tau	τ from method $14a_\tau$ [Gyr]
121	EBV_14a_tau	$E(B-V)$ from method $14a_\tau$ [mag]
122	SFR_14a_tau	SFR from method $14a_\tau$ [$M_\odot\ {\rm yr}^{-1}$]
123	q_14a_tau	Fit quality (1 = Best; 2 = Good; 3 = Bad/No solution) from method $14a_\tau$

(This table is available in its entirety in machine-readable form.)

References

Abazajian, K. N., Adelman-McCarthy, J. K., Agüeros, M. A., et al. 2009, ApJS, 182, 543
Acquaviva, V., Gawiser, E., & Guaita, L. 2012, in IAU Symp. 284 The Spectral Energy Distribution of Galaxies, ed. R. J. Tuffs & C. C. Popescu (Cambridge: Cambridge Univ. Press), 42
Ashby, M. L. N., Willner, S. P., Fazio, G. G., et al. 2013, ApJ, 769, 80
Ashby, M. L. N., Willner, S. P., Fazio, G. G., et al. 2015, ApJS, 218, 33
Barden, M., Häußler, B., Peng, C. Y., McIntosh, D. H., & Guo, Y. 2012, MNRAS, 422, 449
Barmby, P., Huang, J.-S., Ashby, M. L. N., et al. 2008, ApJS, 177, 431
Barro, G., Pérez-González, P. G., Gallego, J., et al. 2011a, ApJS, 193, 13
Barro, G., Pérez-González, P. G., Gallego, J., et al. 2011b, ApJS, 193, 30
Bertin, E., & Arnouts, S. 1996, A&AS, 117, 393
Bielby, R., Hudelot, P., McCracken, H. J., et al. 2012, A&A, 545, A23
Bolzonella, M., Miralles, J.-M., & Pelló, R. 2000, A&A, 363, 476
Bouwens, R. J., Illingworth, G. D., Oesch, P. A., et al. 2015, ApJ, 803, 34
Brammer, G. B., van Dokkum, P. G., & Coppi, P. 2008, ApJ, 686, 1503
Brammer, G. B., van Dokkum, P. G., Franx, M., et al. 2012, ApJS, 200, 13
Brown, M. J. I., Moustakas, J., Smith, J.-D. T., et al. 2014, ApJS, 212, 18
Bruzual, G., & Charlot, S. 2003, MNRAS, 344, 1000
Bundy, K., Ellis, R. S., Conselice, C. J., et al. 2006, ApJ, 651, 120
Caldwell, J. A. R., McIntosh, D. H., Rix, H.-W., et al. 2008, ApJS, 174, 136

Calzetti, D., Armus, L., Bohlin, R. C., et al. 2000, ApJ, 533, 682
Cardamone, C. N., van Dokkum, P. G., Urry, C. M., et al. 2010, ApJS, 189, 270
Cardelli, J. A., Clayton, G. C., & Mathis, J. S. 1989, ApJ, 345, 245
Chabrier, G. 2003, ApJL, 586, L133
Cirasuolo, M., McLure, R. J., Dunlop, J. S., et al. 2007, MNRAS, 380, 585
Coil, A. L., Davis, M., Madgwick, D. S., et al. 2004, ApJ, 609, 525
Conselice, C. J., Bundy, K., U, Vivian, et al. 2008, MNRAS, 383, 1366
Cooper, M. C., Aird, J. A., Coil, A. L., et al. 2011, ApJS, 193, 14
Cooper, M. C., Griffith, R. L., Newman, J. A., et al. 2012, MNRAS, 419, 3018
Cooper, M. C., Newman, J. A., Croton, D. J., et al. 2006, MNRAS, 370, 198
Cuillandre, J.-C., Starr, B., Isani, S., McDonald, J. S., & Luppino, G. 2001, in ASP Conf. Ser. 232, The New Era of Wide Field Astronomy, ed. R. Clowes, A. Adamson, & G. Bromage (San Francisco, CA: ASP), 398
Dahlen, T., Mobasher, B., Faber, S. M., et al. 2013, ApJ, 775, 93
Davis, M., Guhathakurta, P., Konidaris, N. P., et al. 2007, ApJL, 660, L1
de Vaucouleurs, G. 1948, AnAp, 11, 247
Donley, J. L., Koekemoer, A. M., Brusa, M., et al. 2012, ApJ, 748, 142
Duncan, K., Conselice, C. J., Mortlock, A., et al. 2014, MNRAS, 444, 2960
Fazio, G. G., Hora, J. L., Allen, L. E., et al. 2004, ApJS, 154, 10
Fernández-Soto, A., Lanzetta, K. M., & Yahil, A. 1999, ApJ, 513, 34
Finkelstein, S. L., Ryan, R. E., Jr., Papovich, C., et al. 2015, ApJ, 810, 71
Fioc, M., & Rocca-Volmerange, B. 1997, A&A, 326, 950
Fitzpatrick, E. L. 1999, PASP, 111, 63
Galametz, A., Grazian, A., Fontana, A., et al. 2013, ApJS, 206, 10
Gardner, J. P., Cowie, L. L., & Wainscoat, R. J. 1993, ApJL, 415, L9
Giavalisco, M., Ferguson, H. C., Koekemoer, A. M., et al. 2004, ApJL, 600, L93
Graham, A. W., & Driver, S. P. 2005, PASA, 22, 118
Gray, M. E., Wolf, C., Barden, M., et al. 2009, MNRAS, 393, 1275
Grazian, A., Fontana, A., de Santis, C., et al. 2006, A&A, 449, 951
Grazian, A., Fontana, A., Santini, P., et al. 2015, A&A, 575, A96
Grogin, N. A., Kocevski, D. D., Faber, S. M., et al. 2011, ApJS, 197, 35
Guo, Y., Ferguson, H. C., Giavalisco, M., et al. 2013, ApJS, 207, 24
Gwyn, S. D. J. 2008, PASP, 120, 212
Gwyn, S. D. J. 2012, AJ, 143, 38
Hsu, L.-T., Salvato, M., Nandra, K., et al. 2014, ApJ, 796, 60
Ilbert, O., Arnouts, S., McCracken, H. J., et al. 2006, A&A, 457, 841
Ivison, R. J., Chapman, S. C., Faber, S. M., et al. 2007, ApJL, 660, L77
Koekemoer, A. M., Faber, S. M., Ferguson, H. C., et al. 2011, ApJS, 197, 36
Kriek, M., van Dokkum, P. G., Labbé, I., et al. 2009, ApJ, 700, 221
Kron, R. G. 1980, ApJS, 43, 305
Labbé, I., Bouwens, R., Illingworth, G. D., & Franx, M. 2006, ApJL, 649, L67
Labbé, I., Franx, M., Rudnick, G., et al. 2003, AJ, 125, 1107
Labbé, I., Huang, J., Franx, M., et al. 2005, ApJL, 624, L81
Labbé, I., Oesch, P. A., Bouwens, R. J., et al. 2013, ApJL, 777, L19
Laidler, V. G., Papovich, C., Grogin, N. A., et al. 2007, PASP, 119, 1325
Laird, E. S., Nandra, K., Georgakakis, A., et al. 2009, ApJS, 180, 102
Lawrence, A., Warren, S. J., Almaini, O., et al. 2007, MNRAS, 379, 1599
Lee, K.-S., Ferguson, H. C., Wiklind, T., et al. 2012, ApJ, 752, 66
Lee, S.-K., Ferguson, H. C., Somerville, R. S., Wiklind, T., & Giavalisco, M. 2010, ApJ, 725, 1644
Lejeune, T., Cuisinier, F., & Buser, R. 1997, A&AS, 125, 229
Lejeune, T., Cuisinier, F., & Buser, R. 1998, A&AS, 130, 65
Lotz, J. M., Davis, M., Faber, S. M., et al. 2008, ApJ, 672, 177
Lutz, D., Poglitsch, A., Altieri, B., et al. 2011, A&A, 532, A90
Maraston, C. 2005, MNRAS, 362, 799
Mobasher, B., Dahlen, T., Ferguson, H. C., et al. 2015, ApJ, 808, 101
Monet, D. G., Levine, S. E., Canzian, B., et al. 2003, AJ, 125, 984
Mortlock, A., Conselice, C. J., Hartley, W. G., et al. 2015, MNRAS, 447, 2
Muzzin, A., Marchesini, D., Stefanon, M., et al. 2013, ApJS, 206, 8
Nayyeri, H., Hemmati, S., Mobasher, B., et al. 2017, ApJS, 228, 7
Nandra, K., Laird, E. S., Adelberger, K., et al. 2005, MNRAS, 356, 568
Nandra, K., Laird, E. S., Aird, J. A., et al. 2015, ApJS, 220, 10
Newman, J. A., Cooper, M. C., Davis, M., et al. 2013, ApJS, 208, 5
Oesch, P. A., van Dokkum, P. G., Illingworth, G. D., et al. 2015, ApJL, 804, L30
Oliver, S. J., Wang, L., Smith, A. J., et al. 2010, A&A, 518, L21
Papovich, C., Dickinson, M., & Ferguson, H. C. 2001, ApJ, 559, 620
Pérez-González, P. G., Rieke, G. H., Villar, V., et al. 2008, ApJ, 675, 234
Rhodes, J., Refregier, A., & Groth, E. J. 2000, ApJ, 536, 79
Roeser, S., Demleitner, M., & Schilbach, E. 2010, AJ, 139, 2440
Salpeter, E. E. 1955, ApJ, 121, 161
Santini, P., Ferguson, H. C., Fontana, A., et al. 2015, ApJ, 801, 97
Schaerer, D., & de Barros, S. 2009, A&A, 502, 423
Scoville, N., Aussel, H., Brusa, M., et al. 2007, ApJS, 172, 1
Skelton, R. E., Whitaker, K. E., Momcheva, I. G., et al. 2014, ApJS, 214, 24
Skrutskie, M. F., Cutri, R. M., Stiening, R., et al. 2006, AJ, 131, 1163
Stefanon, M., Marchesini, D., Muzzin, A., et al. 2015, ApJ, 803, 11
Stern, D., Eisenhardt, P., Gorjian, V., et al. 2005, ApJ, 631, 163
Stetson, P. B. 1987, PASP, 99, 191
Stoughton, C., Lupton, R. H., Bernardi, M., et al. 2002, AJ, 123, 485
Tody, D. 1986, Proc. SPIE, 627, 733
Tody, D. 1993, in ASP Conf. Ser. 52, Astronomical Data Analysis Software and Systems II, ed. R. J. Hanisch, R. J. V. Brissenden, & J. Barnes (San Francisco, CA: ASP), 173
Tomczak, A. R., Quadri, R. F., Tran, K.-V. H., et al. 2014, ApJ, 783, 85
van de Sande, J., Kriek, M., Franx, M., et al. 2013, ApJ, 771, 85
van Dokkum, P. G., Brammer, G., Fumagalli, M., et al. 2011, ApJL, 743, L15
van Dokkum, P. G., Labbé, I., Marchesini, D., et al. 2009, PASP, 121, 2
Westera, P., Lejeune, T., Buser, R., Cuisinier, F., & Bruzual, G. 2002, A&A, 381, 524
Whitaker, K. E., Labbé, I., van Dokkum, P. G., et al. 2011, ApJ, 735, 86
Wiklind, T., Dickinson, M., Ferguson, H. C., et al. 2008, ApJ, 676, 781
Willner, S. P., Coil, A. L., Goss, W. M., et al. 2006, AJ, 132, 2159
Yan, H., Finkelstein, S. L., Huang, K.-H., et al. 2012, ApJ, 761, 177